Fluid Dynamics &
Materials Processing

Tech Science Press

http://doi.org/10.32604/fdmp.2026.082520

ARTICLE

# A Combined Asymptotic and Characteristic-Based Computational Framework for Exit-Plane Disturbance Response in Solid Rocket Motor Chambers

**Abdelkarim Hegab[1,*], Faisal Albatati[1], Ahmad Hussain[2], Asad A. Zaidi[3,*], Abdullah Abuhabaya[1] and Ragab A. El-Sehiemy[4,5]**

[1]Mechanical Engineering Department, Faculty of Engineering, King Abdulaziz University, Rabigh, Saudi Arabia
[2]Department of Mechanical Engineering, DHA Suffa University, Karachi, Pakistan
[3]Department of Mechanical Engineering, Faculty of Engineering, Islamic University of Madinah, Madinah, Saudi Arabia
[4]Electrical Engineering Department, Faculty of Engineering, Kafrelshiekh University, Kafr El-Sheikh, Egypt
[5]Széchenyi István University, Egyetem tér 1., Győr, Hungary
*Corresponding Authors: Abdelkarim Hegab. Email: amhegab@kau.edu.sa; Asad A. Zaidi. Email: sali@iu.edu.sa

Received: 17 March 2026; Accepted: 08 June 2026; Published: 30 June 2026

**ABSTRACT:** A combined asymptotic and characteristic-based computational framework is developed to investigate unsteady compressible flow response in solid rocket motor (SRM) chambers subjected to exit-plane disturbances and steady sidewall mass injection. The formulation integrates a low-Mach-number asymptotic reduction of the governing equations with a time-accurate numerical solution of the parabolized Navier–Stokes equations, employing characteristic-based boundary conditions to ensure physically consistent wave reflection and transmission at chamber boundaries. Controlled exit-plane pressure forcing is imposed under non-resonant and near-resonant conditions to examine acoustic–vorticity coupling mechanisms within slender SRM geometries. The computational framework is verified and validated against analytical solutions and available experimental measurements for canonical duct configurations, demonstrating accurate pressure wave prediction and stable long-time integration over multiple acoustic cycles. The validated model is subsequently applied to configurations with sidewall mass injection, where interaction between injected flow and acoustic oscillations generates rotational structures that progressively penetrate the chamber cross-section. Parametric investigations reveal strong Reynolds-number dependence of vorticity amplitude, wave penetration depth, and transient flow reversal behavior. Increasing Reynolds number reduces viscous attenuation and promotes sustained wave–vorticity interaction, while weakly nonlinear modulation introduces higher harmonic content in the acoustic response. Despite complex velocity and vorticity structures, transverse pressure gradients remain negligible for slender chamber configurations, consistent with asymptotic predictions.

**KEYWORDS:** Solid rocket motor; aeroacoustics; computational fluid dynamics; characteristic boundary conditions; acoustic–vorticity interaction; Reynolds-number effects; exit-plane forcing; unsteady compressible flow

## 1 Introduction

The dynamic interaction between acoustic waves and fluid motion plays a critical role in the stability and performance of propulsion systems, particularly in solid rocket motor (SRM) chambers [1]. Pressure oscillations generated within the chamber can couple with the internal flow field, leading to complex wave–flow interactions that may amplify unsteady behavior and trigger acoustic instabilities [2]. These instabilities can result in excessive structural loading, reduced propulsion efficiency, and, in severe cases, catastrophic

failure. Consequently, understanding and predicting the coupled acoustic–fluid dynamic response of rocket chambers under realistic boundary disturbances remains a central challenge in propulsion system design [3,4].

Modern propulsion research increasingly relies on advanced computational modeling to investigate these phenomena, driven by continuous improvements in numerical methods and computational resources [5]. High-fidelity simulations enable detailed examination of unsteady compressible flows, wave propagation, and boundary-induced disturbances that are difficult to isolate experimentally [6]. In this context, computational fluid dynamics (CFD) has become an indispensable tool for analyzing acoustic–flow interactions and for assessing the stability characteristics of propulsion chambers under a wide range of operating conditions [7,8].

Designing high-performance solid propellant motors requires an integrated understanding of multiple interacting physical processes, including solid propellant combustion, internal chamber flow, nozzle dynamics, and exhaust plume behavior [9]. A complete simulation of the full SRM system involves coupled reactive, turbulent, and multiphase flows spanning a broad range of spatial and temporal scales, making such analyses exceptionally challenging [10,11]. As a result, much of the existing literature has focused on simplified or isolated submodels, aiming to elucidate fundamental mechanisms governing acoustic wave propagation and fluid dynamic response within idealized chamber geometries [12].

Within SRM chambers, pressure oscillations are often described in terms of eigenfunctions associated with the acoustic modes of the cavity. When forced disturbances interact with these natural modes, energy exchange mechanisms may arise, potentially leading to wave steepening, harmonic generation, and nonlinear acoustic behavior [13,14]. Early theoretical and experimental investigations demonstrated that forced oscillations in ducts and resonant cavities can give rise to shock-like waveforms and strong nonlinear effects, particularly near resonance conditions [15–18]. Subsequent studies further examined the influence of boundary geometry, end conditions, and partial openness on acoustic damping, wave radiation, and shock formation [19–22].

More recently, analytical and computational studies have explored the role of endwall and exit-plane disturbances in generating unsteady flow features, including vorticity production and temperature nonuniformities within channels and cavities [23–26]. These investigations highlighted the importance of boundary-induced forcing in shaping the internal flow field and emphasized the need for accurate boundary condition treatments in numerical simulations. In particular, characteristic-based approaches have been shown to significantly improve the representation of wave reflection and transmission at computational boundaries, enabling stable long-time integration of unsteady compressible flows [27–30].

Despite these advances, several important gaps remain. Many existing studies either focus exclusively on analytical formulations or rely solely on numerical simulations, without systematically integrating both approaches into a unified modeling framework. Furthermore, the combined effects of exit-plane acoustic forcing and steady sidewall mass injection—a configuration relevant to solid rocket motor chambers—have received limited attention, particularly under non-resonant and weakly nonlinear conditions [31,32]. The manner in which such forcing generates and sustains rotational flow structures, and how these structures evolve across the chamber cross-section over long time scales, is not yet fully understood [33].

Recent studies [34–37] have investigated acoustic–flow interaction, combustion instability, and vortex–acoustic coupling in solid rocket motor chambers using high-fidelity numerical simulations, combustion-response models, and simplified acoustic formulations. However, these approaches are typically developed independently and do not provide a unified framework that combines analytical acoustic interpretation with time-accurate numerical simulation under controlled boundary forcing. As a result, the interaction between

exit-plane disturbances and sidewall mass injection, particularly under weakly nonlinear conditions, remains insufficiently explored. To further clarify the research gap and highlight the novelty of the present work, a comparative summary of recent approaches and their limitations relative to the proposed framework is provided in Table 1.

**Table 1:** Comparison of recent approaches and the present framework.

| Approach | Representative Study | Main Focus | Limitation | Present Work |
|---|---|---|---|---|
| Combustion-response/thermoacoustic instability model | Xu et al. (2024) [34] | Triggered thermoacoustic instability driven by linear and nonlinear combustion response in SRMs | Focuses mainly on combustion-response-driven instability; less emphasis on asymptotic interpretation of exit-plane forcing with sidewall injection | Integrates low-Mach asymptotic analysis with time-accurate numerical simulation to interpret acoustic–flow coupling |
| Two-phase CFD/LES model | Huo et al. (2024) [35] | Pressure oscillations caused by vortex–acoustic coupling in SRM chambers with two-phase flow interaction | Provides detailed numerical prediction but mainly remains CFD-based and computationally intensive | Uses controlled forcing to isolate fundamental acoustic–vorticity mechanisms with lower computational complexity |
| Large-aspect-ratio SRM LES model | Xi et al. (2025) [37] | Vortex-induced pressure oscillation and suppression in large-aspect-ratio SRMs | Focuses on pressure oscillation suppression; does not combine asymptotic acoustic theory with characteristic-based computation | Examines exit-plane disturbance response and Reynolds-number-dependent vorticity generation in a unified analytical–computational framework |
| Characteristic-boundary-condition model | Recent NSCBC assessment studies [36] | Reduction of artificial wave reflections in compressible-flow simulations | Focuses mainly on boundary treatment; not directly linked with low-Mach asymptotic acoustic modeling in SRM chambers | Combines characteristic-based boundary treatment with asymptotic acoustic interpretation and full numerical solution |
| Present framework | Present study | Exit-plane disturbance response, sidewall mass injection, acoustic–vorticity interaction, and weakly nonlinear behavior | Non-reactive and two-dimensional formulation | Provides a stable, interpretable, and computationally efficient framework for long-time acoustic–flow simulations |

The present study introduces a unified modeling framework that systematically combines low-Mach-number asymptotic analysis with a time-accurate numerical solution of the parabolized Navier–Stokes equations to investigate unsteady compressible flows in solid rocket motor chambers. Unlike prior studies that rely exclusively on either analytical or computational approaches, the proposed formulation integrates both methodologies within a consistent theoretical and numerical structure. This integration enables direct interpretation of the underlying acoustic mechanisms while retaining the flexibility and predictive capability of high-fidelity computational simulations. Compared with classical approaches based solely on the Navier–Stokes equations, the present framework provides both numerical prediction and analytical interpretation of the acoustic field. While CFD simulations resolve the full unsteady flow, they do not directly reveal

acoustic modal structure or weakly nonlinear behavior. The low-Mach-number asymptotic formulation used here complements the numerical solution by providing physical insight into wave propagation and modal interactions. This combined approach therefore enables a more complete understanding of acoustic–flow coupling mechanisms.

A key contribution of this work lies in the implementation of characteristic-based boundary conditions to accurately represent wave reflection and transmission at the chamber head and exit planes. This treatment significantly improves numerical stability and allows long-time simulations over multiple acoustic cycles without spurious reflections or artificial damping. As a result, the framework is well suited for examining forced acoustic responses under non-resonant and near-resonant conditions, where weakly nonlinear effects and boundary-induced disturbances play a dominant role.

Furthermore, the study provides a detailed computational investigation of acoustic–vorticity coupling arising from exit-plane pressure forcing in the presence of steady sidewall mass injection. The interaction between injected flow and acoustically induced unsteadiness is shown to generate rotational flow structures that penetrate progressively across the chamber cross-section. Through systematic parametric analysis, the influence of the characteristic Reynolds number on vorticity amplitude, wave penetration depth, and flow reversal behavior is quantified, revealing distinct trends that are not evident from purely analytical treatments.

Collectively, these contributions establish a robust and versatile computational framework for analyzing unsteady flow–acoustic interactions in propulsion-related configurations. The results offer new insight into the role of boundary forcing and flow parameters in shaping internal chamber dynamics and provide a foundation for improved predictive modeling of acoustic–flow interaction phenomena in solid rocket motor chambers.

Accordingly, the objectives of the present study are to develop a robust computational framework that captures weakly nonlinear acoustic behavior in solid rocket motor chambers subjected to exit-plane disturbances and steady sidewall mass injection, to verify and validate the proposed methodology against available analytical and experimental benchmarks, and to systematically examine the interaction between acoustically induced unsteadiness and injected flow. Particular emphasis is placed on quantifying the influence of the characteristic Reynolds number on unsteady vorticity generation, wave penetration depth, and flow reversal behavior within slender chamber geometries. Through these objectives, the study aims to provide physically grounded insight into acoustic–flow interaction mechanisms and to enhance predictive modeling capabilities for unsteady propulsion-related flows.

## 2 Mathematical Model

### *2.1 Physical Configuration and Flow Assumptions*

The physical configuration considered in this study represents an idealized two-dimensional solid rocket motor chamber designed to isolate and examine fundamental acoustic–flow interaction mechanisms. As illustrated in Fig. 1, the chamber consists of a slender rectangular duct of length $L'$ and half-height $H'$, yielding a large aspect ratio $\alpha = L'/H'$, which is representative of practical solid rocket motor geometries. The chamber is closed at the head end and open at the exit plane, where controlled unsteady forcing is imposed.

To match the mass addition associated with solid propellant combustion, a steady and spatially uniform mass injection velocity is prescribed at the upper and lower chamber walls. This sidewall injection generates a mean axial flow directed toward the exit plane while maintaining geometric simplicity. At the exit, a time-dependent pressure disturbance is imposed to excite acoustic wave motion within the chamber. This forcing

is used to generate controlled non-resonant and near-resonant acoustic responses, allowing systematic investigation of wave propagation and flow–acoustic coupling.

The working fluid is assumed to be a calorically perfect gas with constant thermophysical properties. The flow is considered compressible and unsteady, while operating in a low Mach number regime characteristic of internal acoustic motion in solid rocket motor chambers. Viscous and thermal diffusion effects are retained to enable accurate representation of boundary-layer behavior and vorticity generation near the injection surfaces. Gravitational effects are neglected.

To focus on the dominant acoustic and flow mechanisms, the analysis is restricted to two-dimensional motion. This assumption is appropriate for capturing the primary longitudinal acoustic modes and the associated transverse vorticity dynamics in slender chambers. The present configuration thus provides a controlled and physically meaningful framework for examining the interaction between exit-plane acoustic forcing, sidewall mass injection, and unsteady flow development.

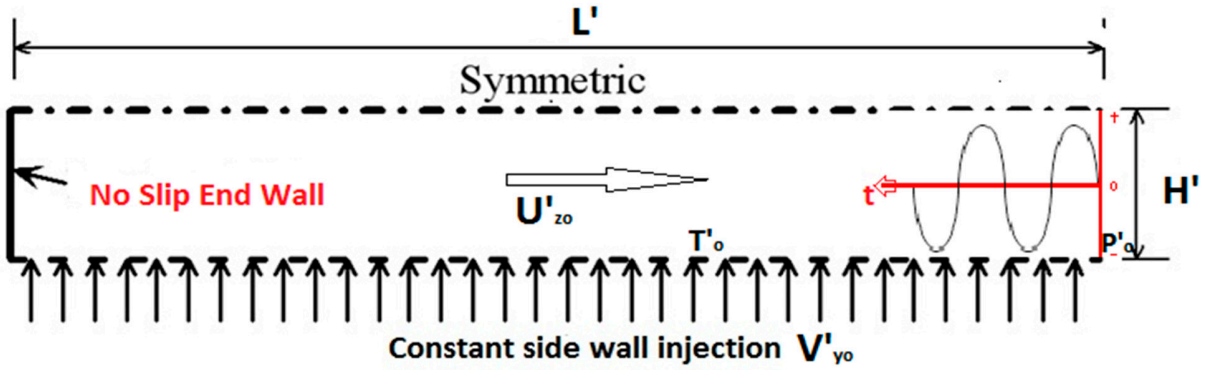


**Figure 1:** Simulated solid rocket motor chamber with constant mass injection from the sidewall and exit-plane disturbances.

### *2.2 Governing Equations and Non-Dimensionalization*

The unsteady flow inside the chamber is described using the complete compressible governing equations for a calorically perfect gas. These equations account for viscous effects and thermal conduction and are employed to model the coupled acoustic and fluid dynamic behavior generated by sidewall mass injection and exit-plane disturbances. The non-dimensional governing equations used in the present study are given in Eqs. (1)–(5) [30]:

$$\frac{\partial \rho}{\partial t} + M\left\{ \frac{\partial \rho u}{\partial x} + \frac{\partial \rho v}{\partial y} + \frac{\partial \rho w}{\partial z} \right\} = 0 \tag{1}$$

$$\rho\left\{ \frac{\partial u}{\partial t} + M\left( u\frac{\partial u}{\partial x} + v\frac{\partial u}{\partial y} + w\frac{\partial u}{\partial z} \right) \right\} = -\frac{1}{\gamma M}\frac{\partial \rho}{\partial x} + \frac{\delta^2}{R_{ed}}\left( \frac{\partial^2 u}{\partial y^2} + \frac{1}{\delta^2}\frac{\partial^2 u}{\partial x^2} + \frac{\partial^2 u}{\partial z^2} \right) \tag{2}$$

$$\frac{\gamma M}{\delta^2}\rho\left\{ \frac{\partial v}{\partial t} + M\left( u\frac{\partial v}{\partial x} + v\frac{\partial v}{\partial y} + w\frac{\partial v}{\partial z} \right) \right\} = -\frac{\partial \rho}{\partial y} + \frac{\gamma M}{R_{ed}}\left( \frac{\partial^2 v}{\partial y^2} + \frac{1}{\delta^2}\frac{\partial^2 v}{\partial x^2} + \frac{\partial^2 v}{\partial z^2} \right) \tag{3}$$

$$\frac{\gamma M}{\delta^2}\rho\left\{ \frac{\partial w}{\partial t} + M\left( u\frac{\partial w}{\partial x} + v\frac{\partial w}{\partial y} + w\frac{\partial w}{\partial z} \right) \right\} = -\frac{\partial \rho}{\partial z} + \frac{\gamma M}{R_{ed}}\left( \frac{\partial^2 w}{\partial y^2} + \frac{1}{\delta^2}\frac{\partial^2 w}{\partial x^2} + \frac{\partial^2 w}{\partial z^2} \right)$$

$$\rho\left\{\frac{\partial T}{\partial t}+M\left(u\frac{\partial T}{\partial x}+v\frac{\partial T}{\partial y}+w\frac{\partial T}{\partial z}\right)\right\} = -(\gamma-1)M\rho\left(\frac{\partial u}{\partial x}+\frac{\partial v}{\partial y}+\frac{\partial w}{\partial z}\right)+\frac{\gamma\delta^2}{P_rR_{ed}}\left(\frac{\partial^2 T}{\partial y^2}+\frac{1}{\delta^2}\frac{\partial^2 T}{\partial x^2}+\frac{\partial^2 T}{\partial z^2}\right) \tag{4}$$

$$P = \rho T \tag{5}$$

In Eqs. (1)–(5), $x$, $y$, and $z$ denote the dimensionless spatial coordinates in the axial, transverse, and spanwise directions, respectively, while $t$ represents dimensionless time. The variables $u$, $v$, and $w$ are the dimensionless velocity components in the $x$-, $y$-, and $z$-directions, respectively; $p$, $\rho$, and $T$ denote the dimensionless pressure, density, and temperature; $\gamma$ is the specific heat ratio; $M$ is the characteristic Mach number; $R_{ed}$ is the Reynolds number; $P_r$ is the Prandtl number; and $\delta$ represents the chamber aspect-ratio scaling parameter. The quantity $E_t$ denotes the total energy, and the equation of state is given by Eq. (5).

The chamber is initially filled with a quiescent gas characterized by the reference pressure $P_o^{'}$, reference temperature $T_o^{'}$, and corresponding reference density. A constant sidewall mass injection velocity $V_{yo}^{'}$ is prescribed at the upper and lower chamber walls to mimic steady propellant burning. This injection generates a characteristic axial velocity $U_{zo}^{'}$ within the chamber. A time-dependent pressure disturbance is imposed at the exit plane to excite acoustic wave motion, while the head end of the chamber is treated as an impermeable boundary.

To facilitate analysis and enable comparison between analytical and computational results, the governing equations are non-dimensionalized using the reference quantities defined in Eqs. (6) and (7). The characteristic acoustic time scale is defined as $t_a^{'} = L'/C_o^{'}$, and the chamber aspect ratio is given by $\alpha = \mathrm{L}'/\mathrm{H}'$. The resulting non-dimensional formulation introduces the characteristic Mach number, Reynolds number, and Prandtl number, as defined in Eq. (8).

$$p = \frac{p'}{p_o^{'}}, \rho = \frac{\rho'}{\rho_o^{'}}, T = \frac{T'}{T_o^{'}}, u = \frac{u'}{U_R^{'}}, v = \frac{v'}{\left(U_R^{'}/\delta\right)}, w = \frac{w'}{\left(U_R^{'}/\delta\right)} \tag{6}$$

$$x = \frac{x'}{L'}, y = \frac{y'}{H'}, z = \frac{z'}{H'}, t = \frac{t'}{t_a^{'}} \tag{7}$$

$$M = \frac{U_R^{'}}{C_o^{'}}, P_R = \frac{\mu_o^{'}C_{PO}^{'}}{k_o^{'}}, R_e = \frac{\rho_o^{'}U_R^{'}L'}{\mu_o^{'}}, R_{EA} = \frac{R_e}{M} \tag{8}$$

The present analysis is conducted under conditions where the characteristic Mach number is small, while the Reynolds number is sufficiently large to allow thin viscous boundary layers to develop along the chamber walls. Under these assumptions, the flow exhibits weak compressibility effects associated with acoustic wave propagation, while viscous and thermal diffusion primarily influence the near-wall regions. These conditions are representative of internal acoustic motion in solid rocket motor chambers.

The non-dimensional governing equations form the basis for both the asymptotic acoustic analysis and the numerical simulations presented in subsequent sections. Detailed expressions for the governing equations, non-dimensional variables, and characteristic flow parameters are provided in Eqs. (1)–(8) and are not repeated here for brevity.

The governing equations are closed by specifying the initial conditions, head-end boundary condition, exit-plane pressure forcing, and wall conditions, which define the physical problem considered in this

study. These conditions describe a quiescent initial state, an impermeable head end, uniform sidewall mass injection, and a prescribed time-dependent pressure disturbance at the exit plane. The complete mathematical expressions for the initial and boundary conditions are given in Eqs. (9)–(12) and are provided in Appendix A for clarity and completeness.

In general, $\delta \gg 1$, $M \ll 1$, $Re \gg 1$, and $P_r = O(1)$.

Given the definition of $M$ in Eq. (8), and the fact that $U_R^{'}$ is known. The general initial and boundary conditions are as follows:

$$t = 0, p = T = \rho = 1, u = v = w = 0, 0 \leq x \leq 1 \tag{9}$$

$$x = 0, u = 0 \tag{10}$$

$$x = 1, p = 1 + Mf(t) \tag{11}$$

$$y = 0, 1, u = v = w = 0, T = 1 \tag{12}$$

In this model, the core solution for an inviscid acoustic flow is studied first. Then, the asymptotic analysis is extended to describe a thin, viscous, acoustic boundary layer adjacent to the wall.

### *2.3 Asymptotic Acoustic Formulation*

To gain physical insight into the acoustic behavior within the chamber and to support interpretation of the numerical results, an asymptotic analysis is employed under the assumption of low characteristic Mach number and large Reynolds number. This approach allows systematic separation of acoustic motion from the mean flow and viscous effects while retaining the essential coupling mechanisms relevant to exit-plane forcing and sidewall mass injection. The low-Mach-number asymptotic formulation is justified because the present study focuses on small-amplitude acoustic disturbances in an SRM chamber, where the characteristic Mach number is much smaller than unity. This approach simplifies the governing equations while retaining the dominant acoustic mechanisms, including wave propagation, modal response, and weakly nonlinear behavior [38]. It is used here as a complementary analytical tool, together with the full unsteady compressible Navier–Stokes solution, to improve the physical interpretation of the computed acoustic–flow interaction.

The asymptotic formulation is developed by introducing perturbation expansions for the flow variables in terms of the small Mach number parameter, as defined in Eq. (A1). Substitution of these expansions into the governing equations given in Eqs. (1)–(5) yields a hierarchy of equations at successive orders. The resulting leading-order and higher-order relations governing pressure, density, temperature, and velocity fields are summarized in Eqs. (A2)–(A6). These expressions form the basis for deriving the reduced acoustic model applicable to the present low-Mach-number regime.

At the lowest order, the asymptotic analysis leads to a set of linear acoustic equations describing the evolution of pressure and velocity fluctuations within the chamber, as given in Eqs. (A7)–(A11). Combining these relations results in a one-dimensional pressure wave equation governing the acoustic field, presented

in Eq. (13). This equation captures the propagation of acoustic waves driven by exit-plane disturbances while accounting for the geometric confinement imposed by the chamber boundaries.

$$\frac{\partial^2 P_o}{\partial t^2} = \frac{\partial^2 P_o}{\partial x^2} \tag{13}$$

The acoustic problem is closed by applying the initial and boundary conditions defined in Eqs. (9)–(12). In particular, a prescribed time-dependent pressure disturbance is imposed at the exit plane, as specified in Eq. (16), while the head end is treated as an impermeable boundary. The resulting solution for the acoustic pressure field is expressed as a superposition of quasi-steady response and chamber eigenfunctions, with the corresponding expressions provided in Eqs. (A12) and (A13). These solutions describe non-resonant and near-resonant acoustic responses and form the analytical reference against which the numerical results are compared.

The asymptotic formulation further indicates that, under the present assumptions, quadratic nonlinear convective terms do not contribute to intermodal energy transfer at the leading-order approximation, while higher-order effects govern weakly nonlinear behavior over longer time scales. These findings motivate the use of a combined analytical and computational approach to accurately capture both short-time acoustic propagation and long-time flow–acoustic interaction phenomena.

The detailed asymptotic expansions, intermediate governing relations, and analytical solution expressions corresponding to Eqs. (A1)–(A13) are provided in Appendix A. For clarity, only the resulting pressure wave equation (Eq. (13)) and the exit-plane forcing definition (Eq. (16)) are retained in the main text.

$$t = 0, P_o = 0, \frac{\partial P_o}{\partial t} = 0, 0 \le x \le 1 \tag{14}$$

$$x = 0, \frac{\partial P_o}{\partial x} = 0, t > 0 \tag{15}$$

$$x = 1, P_o = f(t) = \varepsilon \sin(\omega t) \tag{16}$$

where $\varepsilon$ is an $O(1)$ coefficient.

### *2.4 Computational Solution*

The numerical solution of the unsteady flow field is obtained by solving the complete two-dimensional compressible Navier–Stokes equations given in Eq. (17), together with the equation of state defined in Eq. (18). The formulation retains viscous and thermal diffusion effects and is suitable for resolving unsteady acoustic phenomena and flow–acoustic interactions within the chamber. The governing equations are discretized using a finite-difference approach and integrated in time through an explicit time-marching scheme. The adopted methodology follows the integrated formulation reported in Refs. [30,39], which has been shown to provide stable and accurate solutions for compressible wave-propagation problems. The numerical solver was developed in-house by the authors using FORTRAN, based on the governing equations and characteristic-based formulation described herein. The developed code and associated numerical framework have been verified and validated in previous related studies involving acoustic/fluid dynamic interaction, vorticity generation, and simulated solid rocket motor chamber flows [40–42].

To facilitate numerical implementation, the governing equations are expressed in wave-mode representation. The detailed wave-mode formulation and associated characteristic variable definitions are provided in Appendix B (Eqs. (A14)–(A21)) and are not repeated here for conciseness.

$$\frac{\partial Q}{\partial t} + \frac{\partial E}{\partial x} + \frac{\partial F}{\partial y} = 0, \tag{17}$$

where $Q$, $E$, and $F$ are column vectors given by the following:

$$Q = \begin{bmatrix} \rho \\ \rho u \\ \rho v \\ E_T \end{bmatrix}$$

$$E = \begin{Bmatrix} M\rho u \\ M\rho u^2 + \frac{1}{\gamma M} p - \frac{4}{3}\frac{M}{R_e} u_x - \frac{1}{3}\frac{M}{R_e} v_y \\ M\rho uv - \frac{M}{R_e} v_x \\ M[E_T + (\gamma - 1)p]u - \frac{\gamma M}{R_e P_r} T_x \end{Bmatrix}$$

$$F = \begin{Bmatrix} M\rho v \\ M\rho uv - \frac{\delta^2 M}{R_e} u_y \\ M\rho v^2 + \frac{\delta^2}{\gamma M} p - \frac{1}{3}\frac{\delta^2 M}{R_e} u_x - \frac{\delta^2}{3}\frac{M}{R_e} v_y \\ M[E_T + (\gamma - 1)p]v - \frac{\gamma \delta^2 M}{R_e P_r} T_y \end{Bmatrix}$$

With the aid of the equation of state for a perfect gas:

$$p = \rho T \tag{18}$$

### *2.5 Exit-Plane Boundary Condition*

At the exit plane, a time-dependent pressure disturbance is prescribed to excite acoustic motion within the chamber, as defined in Eq. (16). This imposed disturbance generates right- and left-running acoustic waves that interact with the internal flow field.

The exit-plane boundary treatment is implemented using characteristic-based relations consistent with the wave-mode formulation introduced in Section 2.4. The complete set of characteristic expressions governing reflected and transmitted wave amplitudes is provided in Appendix B (Eqs. (A22)–(A25)). This formulation ensures accurate representation of wave propagation while minimizing spurious numerical reflections during long-time simulations. In particular, the characteristic-based treatment distinguishes between incoming and outgoing waves, allowing outgoing waves to leave the domain freely while only prescribing physically consistent incoming information. This selective specification prevents non-physical wave reflection at the boundary and improves numerical stability.

### *2.6 Head End Boundary Condition*

The head end of the chamber is treated as an impermeable boundary, consistent with the physical configuration of a closed-end solid rocket motor chamber. This condition enforces zero normal velocity at the boundary and results in reflection of incoming acoustic waves. The characteristic-based implementation used to enforce the impermeable condition is described in Appendix B (Eqs. (A36)–(A42)). These relations ensure compatibility between the boundary treatment and the governing compressible flow equations while preserving numerical stability.

At the head end, the boundary is impermeable, and the normal velocity component vanishes. Under this condition, the transverse characteristic components associated with entropy and shear waves are eliminated, and acoustic wave reflection occurs according to the characteristic compatibility relations. The outgoing and incoming acoustic wave amplitudes are determined consistently using the wave-mode formulation introduced in Section 2.4, while the detailed algebraic expressions governing their computation are provided in Appendix B (Eqs. (A36)–(A42)). This treatment ensures that the reflected acoustic wave re-enters the computational domain in a manner fully compatible with the governing compressible flow equations.

### *2.7 Stability Criteria of Numerical Schemes*

Numerical stability of the time-marching procedure is ensured through appropriate selection of the time-step size. In the present study, stability considerations are governed by the Courant–Friedrichs–Lewy (CFL) condition, which provides a necessary constraint for explicit integration schemes applied to hyperbolic systems of equations.

The time-step size is selected in accordance with the CFL criterion defined in Eq. (19), where the Courant number is maintained below unity to ensure stable numerical integration. This condition accounts for the local wave propagation speed and spatial discretization, thereby preventing numerical instabilities associated with excessive time-step sizes.

Extensive numerical testing was performed to identify an optimal range of Courant numbers that balances numerical stability and computational efficiency. Within this range, the adopted numerical scheme yields accurate resolution of acoustic wave propagation and remains stable over multiple wave cycles. The stability behavior observed in the present simulations is consistent with the guidelines reported in previous studies employing similar numerical formulations.

The stability criterion described above is applied uniformly across all simulations presented in this work and forms an integral part of the overall computational framework.

$$(\Delta t_{CFL})_{i,j} = \frac{1}{\left[M\left(\frac{|u_{i,j}|}{\Delta x}+\frac{|v_{i,j}|}{\Delta y}\right)+C_{i,j}\sqrt{\frac{1}{\Delta x^2}+\frac{\delta^2}{\Delta y^2}}+\frac{3M}{R_e}\left(\frac{1}{\Delta x^2}+\frac{\delta^2}{\Delta y^2}\right)\right]} \tag{19}$$

where $\Delta t = \min\left[\vartheta(\Delta t_{CFL})_{i,j}\right]$ and the Courant number $\vartheta$ is less than one, where the best results are found for $0.5 \leq \vartheta \leq 0.65$.

## 3 Code Validation

To establish the reliability and predictive capability of the computational framework developed in this study, the numerical implementation was validated against both analytical solutions and experimental measurements reported in the literature.

### *3.1 Validation against Experimental Measurements*

The computational model was first validated using experimental data reported by Hegab et al. [40]. The experimental configuration consisted of a cavity with a piston oscillating at the head end and a pressure node located at the exit. Acoustic pressure fields were measured at multiple axial locations using capacitive pressure transducers connected to a computer-based data acquisition system. The motor frequency was controlled through voltage modulation, allowing excitation of the fundamental natural modes of the cavity within the available frequency range (250 Hz).

For validation purposes, the pressure history at x = 0.125, $\varepsilon$ = 0.045, and $\omega$ = 0.52 (f′ = 63.44 Hz) was selected. The comparison between experimental measurements and computational predictions is shown in Fig. 2. The numerical results accurately reproduce both the amplitude and phase characteristics of the measured pressure oscillations, demonstrating that the adopted numerical scheme is capable of capturing the essential acoustic response of the cavity.

The agreement between the computed and experimental pressure-time histories confirms that the characteristic-based boundary treatment and time-marching procedure provide stable and physically consistent solutions over multiple oscillation cycles.

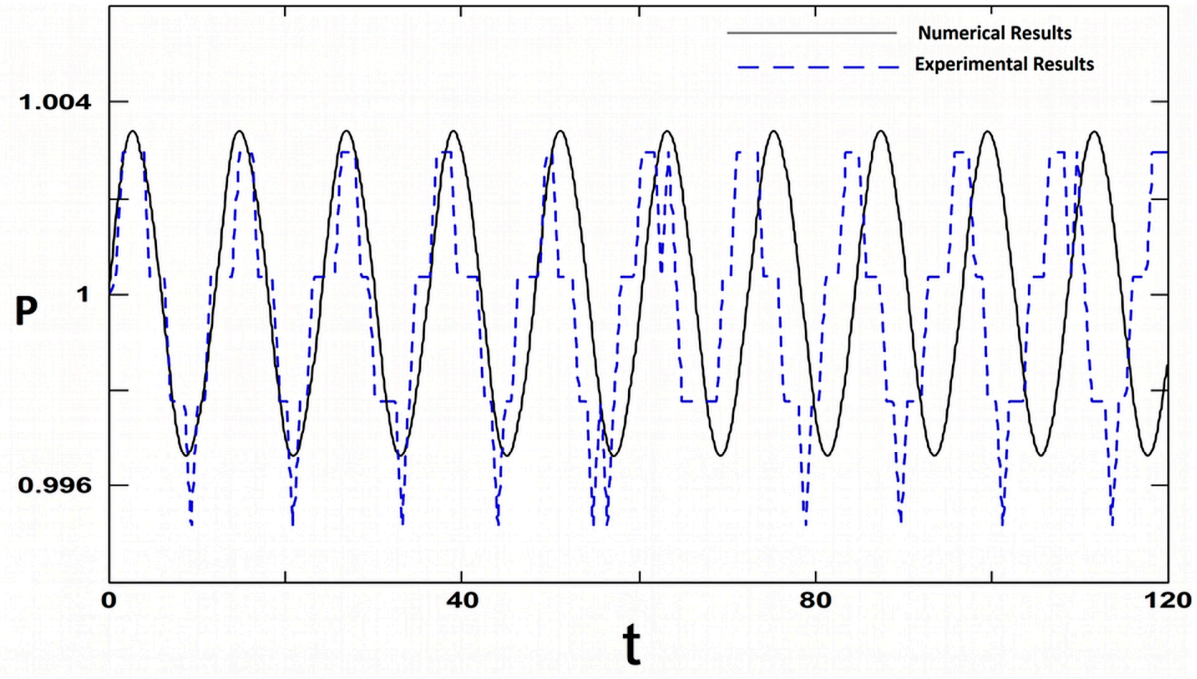


**Figure 2:** Comparison of experimental and computational pressure-time profiles at location: x = 0.125, $\varepsilon$ = 0.045, and $\omega$ = 0.52 (f′ = 63.44 Hz).

### *3.2 Validation of Flow Field Predictions*

In addition to acoustic pressure validation, the developed FORTRAN code has been previously examined using different turbulence models to assess its capability in predicting flow-field behavior under sidewall mass injection conditions. Comparisons reported in earlier studies showed that the RSM v2-f and SST k-$\omega$ turbulence models exhibited strong agreement with experimental observations, as illustrated in Fig. 3.

Fig. 3 presents the spatial distribution of the local friction coefficient along the chamber wall. The results indicate that the flow remains laminar near the head end and transitions to turbulence downstream.

Among the tested models, the v2-f turbulence model most accurately captures the transition behavior and wall-shear distribution. Based on these findings, the v2-f model is adopted in the present simulations involving sidewall injection.

This prior verification supports the robustness of the numerical implementation in resolving both acoustic and viscous flow characteristics within the chamber. To further compare the present computational framework with previously published results, the normalized axial velocity profile at the chamber mid-length was evaluated for the steady sidewall-injection flow. As shown in Fig. 4, the present prediction follows the published velocity-profile trend closely, confirming that the developed code accurately reproduces the mean flow structure before being applied to unsteady acoustic–flow simulations.

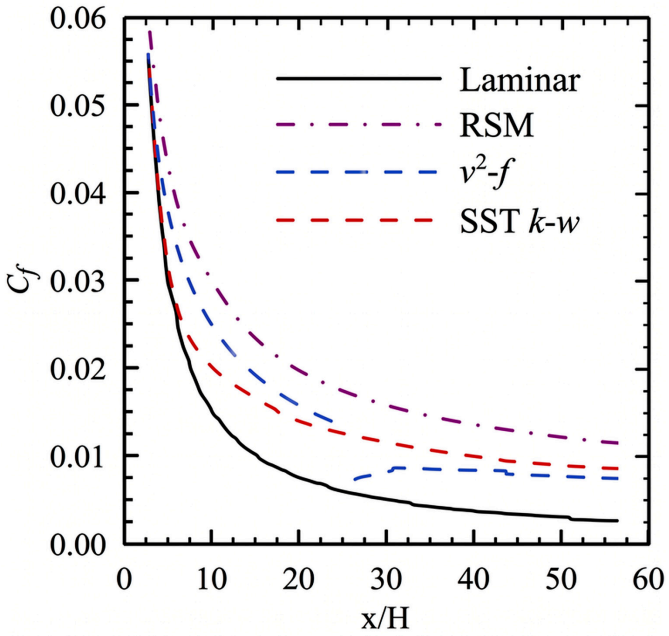


**Figure 3:** Spatial distribution of the local friction coefficient along the chamber wall of the solid rocket motor with sidewall injection.

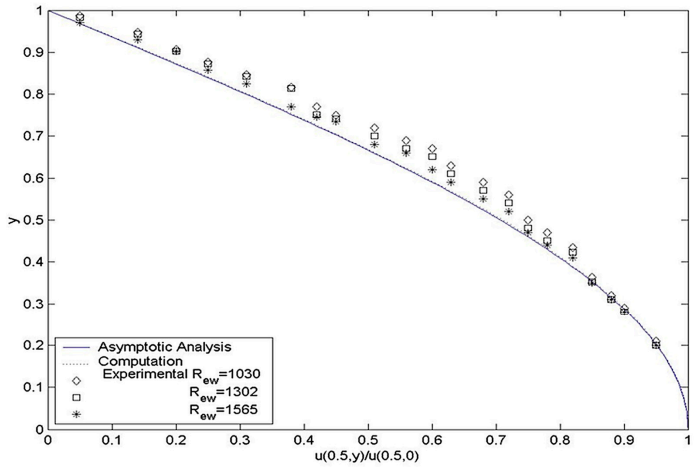


**Figure 4:** Comparison of normalized axial velocity profiles at the mid-length of the chamber for steady sidewall-injection flow with previously published results [40].

### *3.3 Validation of Analytical–Computational Consistency*

Further validation was conducted by comparing computational predictions with the analytical non-resonant acoustic solution derived in Section 2.3. The comparison of perturbed pressure time histories at the chamber mid-length for $\alpha = 1$ is presented in Fig. 5.

The results show excellent agreement between analytical and computational predictions, particularly in capturing the primary harmonic response and the presence of higher harmonic components superimposed on the fundamental mode. Unlike earlier computational implementations reported by Hegab [41] and Hegab et al. [42], where deviations became significant for $t > 20$, the present formulation remains stable and accurate for extended simulation times ($t > 60$). This demonstrates the effectiveness of the adopted characteristic-based boundary condition treatment in reducing numerical diffusion and maintaining solution accuracy over long time intervals.

The strong consistency between analytical and numerical solutions confirms that the computational framework accurately captures both linear acoustic propagation and weakly nonlinear effects under non-resonant forcing conditions.

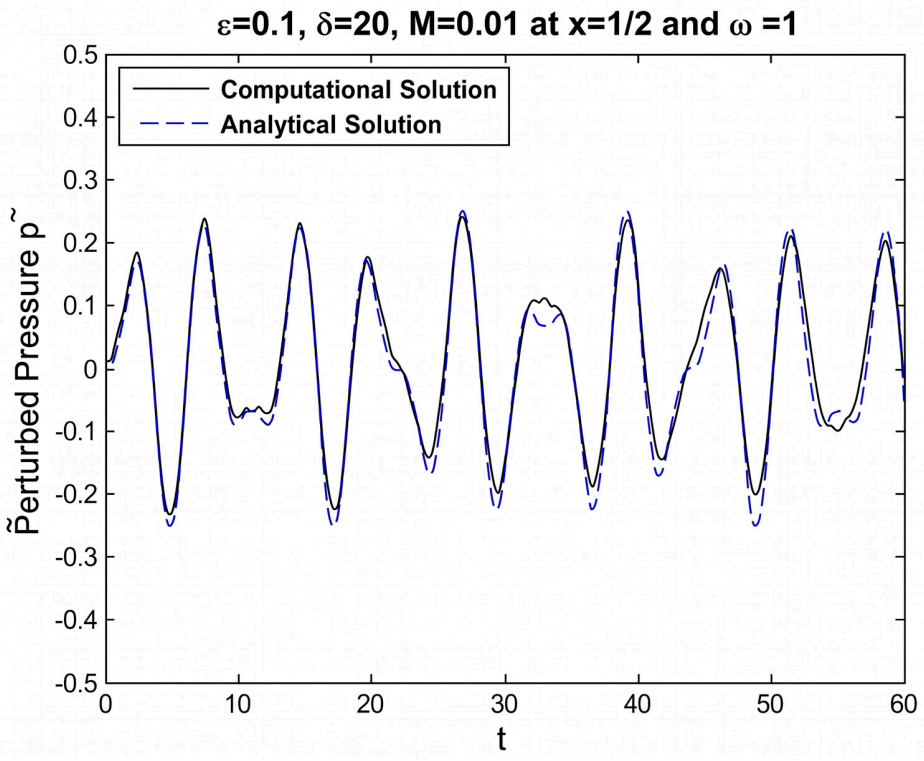


**Figure 5:** Computational versus analytical results for pressure-time history at the mid-length of the chamber for non-resonance solutions.

### *3.4 Discussion of Validation Outcomes*

The combined comparisons with experimental measurements, prior numerical studies, and analytical solutions demonstrate that the developed computational framework provides consistent and physically reliable predictions of unsteady acoustic and flow behavior within the chamber. The numerical scheme accurately reproduces pressure oscillation amplitudes and phase characteristics observed experimentally, while also maintaining long-time stability over multiple acoustic cycles. The agreement between analyt-

ical and computational solutions confirms that the formulation captures the dominant acoustic modes as well as higher harmonic contributions associated with weakly nonlinear behavior. In addition, the validated turbulence modeling approach successfully resolves boundary-layer development and transition behavior under sidewall mass injection conditions. Collectively, these results establish the robustness and predictive capability of the adopted computational methodology and demonstrate strong agreement with previously published experimental, analytical, and numerical studies on acoustic–flow interaction in similar configurations [23–25].

### *3.5 Numerical Consistency and Stability Assessment*

In addition to the validation cases presented above, numerical consistency of the computational framework was assessed through systematic testing of the time-marching procedure and boundary-condition implementation. Particular attention was given to the stability of long-time integration and the preservation of acoustic wave characteristics over multiple oscillation cycles. To provide a quantitative assessment of numerical consistency, the predicted vorticity-front location was compared with the corresponding analytical solution at different time instants. The absolute deviation and percentage variation were calculated, as summarized in Table 2. The percentage variation remains within approximately 6%, indicating that the adopted numerical resolution provides stable and reliable predictions for the present acoustic–flow simulations.

**Table 2:** Mesh sensitivity analysis based on comparison of analytical and computational vorticity-front locations at $M = 0.01$, $Re = 3 \times 10^5$, $\varepsilon = 0.4$, and $\omega = 1$.

| Time | Analytical Vorticity-Front Location | Computational Vorticity-Front Location | Absolute Deviation | Percentage Variation (%) |
|---|---|---|---|---|
| (t = 0) | 1.000 | 1.000 | 0.000 | 0.00 |
| (t = 8) | 0.902 | 0.880 | 0.022 | 2.44 |
| (t = 16) | 0.835 | 0.805 | 0.030 | 3.59 |
| (t = 32) | 0.679 | 0.720 | 0.041 | 6.04 |
| (t = 40) | 0.600 | 0.621 | 0.021 | 3.50 |

Numerical stability was ensured by enforcing the CFL condition, maintaining the Courant number within the range 0.5–0.65, and using a MacCormack-type finite-difference scheme with second-order accuracy in space and time. In addition, the characteristic-based boundary treatment minimized artificial wave reflections at the head and exit boundaries, preventing the accumulation of numerical errors during long-time simulations.

The adopted numerical formulation, combined with the characteristic-based boundary condition treatment described in Section 2, demonstrated stable behavior for extended simulation times without the appearance of spurious oscillations or artificial numerical damping. As observed in Fig. 6, the computational results remain consistent with the analytical solution beyond $t > 60$, indicating that the numerical scheme maintains accuracy over time intervals significantly longer than those reported in earlier implementations [20,26].

Furthermore, the stability criterion defined in Eq. (19) was applied consistently across all simulations to ensure stable time integration. Within the recommended Courant number range, no instability or divergence was observed, and the computed pressure and flow fields remained bounded and physically consistent.

These observations confirm that the adopted spatial discretization, time integration strategy, and characteristic boundary treatment provide a stable and reliable computational framework for simulating unsteady acoustic–flow interactions in the present configuration.

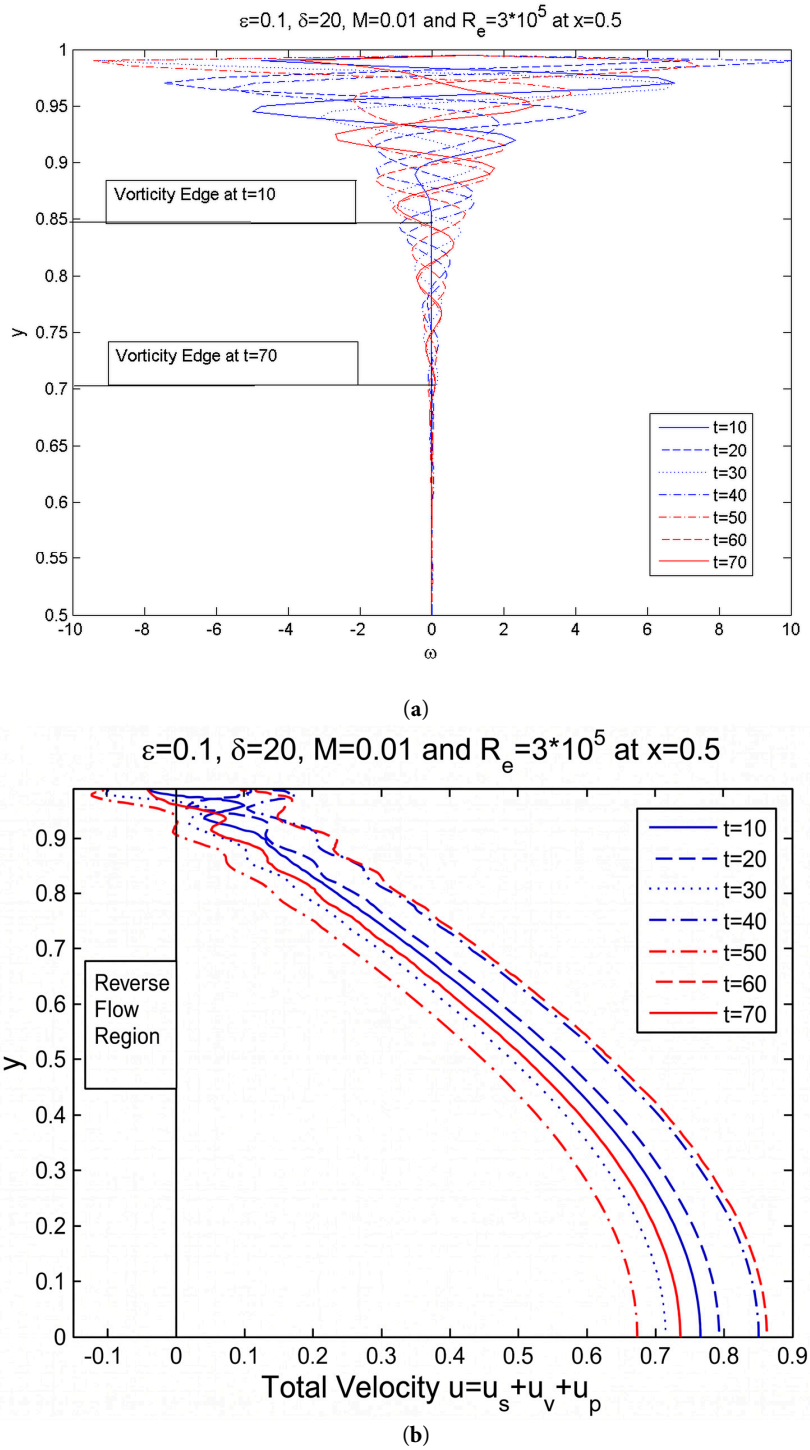


**Figure 6:** Vertical variations of (**a**) unsteady generated vorticity and (**b**) the total velocity component at the mid-length of the chamber at seven different times for the non-resonance solution.

## 4 Results and Discussion

This section presents the computational results obtained using the validated numerical framework described in Section 3. The analysis focuses on the interaction between exit-plane acoustic forcing and steady sidewall mass injection, with particular emphasis on vorticity generation, velocity field evolution, and the influence of the characteristic Reynolds number on unsteady flow development.

### *4.1 Acoustic–Vorticity Interaction Mechanism*

The asymptotic formulation presented in Section 2.3 indicates that, under low-Mach-number conditions, acoustic pressure fluctuations govern the dominant unsteady behavior within the chamber. When steady sidewall mass injection is present, the oscillatory acoustic field interacts with the injected flow, resulting in the generation of rotational motion near the injection surfaces.

The total axial velocity may be decomposed as expressed in Eq. (20), separating the steady, planar, and rotational contributions. The corresponding unsteady vorticity, defined in Eqs. (21) and (22), provides a quantitative measure of rotational flow generation induced by acoustic forcing.

$$u(x, y, t) = u_v(x, y, t) + u_s(x, y) + u_p(x, t) \tag{20}$$

$$\Omega = -\left[\frac{\partial u_v}{\partial y} - \frac{1}{\delta^2}\frac{\partial v_v}{\partial x}\right] \tag{21}$$

$$\Omega = \Omega/(U_{zo}/H) \tag{22}$$

The transverse velocity component defined in Eq. (23) represents the deviation of the instantaneous vertical velocity from the converged steady flow field. This decomposition enables isolation of the unsteady rotational contribution associated with acoustic forcing, thereby facilitating interpretation of the vorticity distributions presented in Figs. 7–10.

$$v_v(x, y, t) = v(x, y, t) - v_s(x, y) \tag{23}$$

Fig. 6a illustrates the vertical distribution of unsteady vorticity at the mid-length of the chamber for the non-resonant solution at seven different times. The results show that rotational motion is initially confined near the injection surfaces and progressively penetrates toward the chamber centerline as time increases. This behavior reflects the coupling between acoustic pressure gradients and the injected shear layer, which amplifies vorticity production near the walls before redistributing it across the cross-section.

Fig. 6b presents the corresponding total velocity component. Oscillatory behavior is observed adjacent to the injection surface, including localized flow reversal. This reverse flow arises from the superposition of the steady injection-induced axial motion and the oscillatory acoustic velocity component. During certain phases of the acoustic cycle, adverse pressure gradients develop along the axial direction, which decelerate the flow and can locally reverse its direction. This effect is strongest near the injection surfaces, where the mean flow is weaker and more sensitive to acoustic forcing, and is further enhanced by the presence of acoustically generated vorticity.

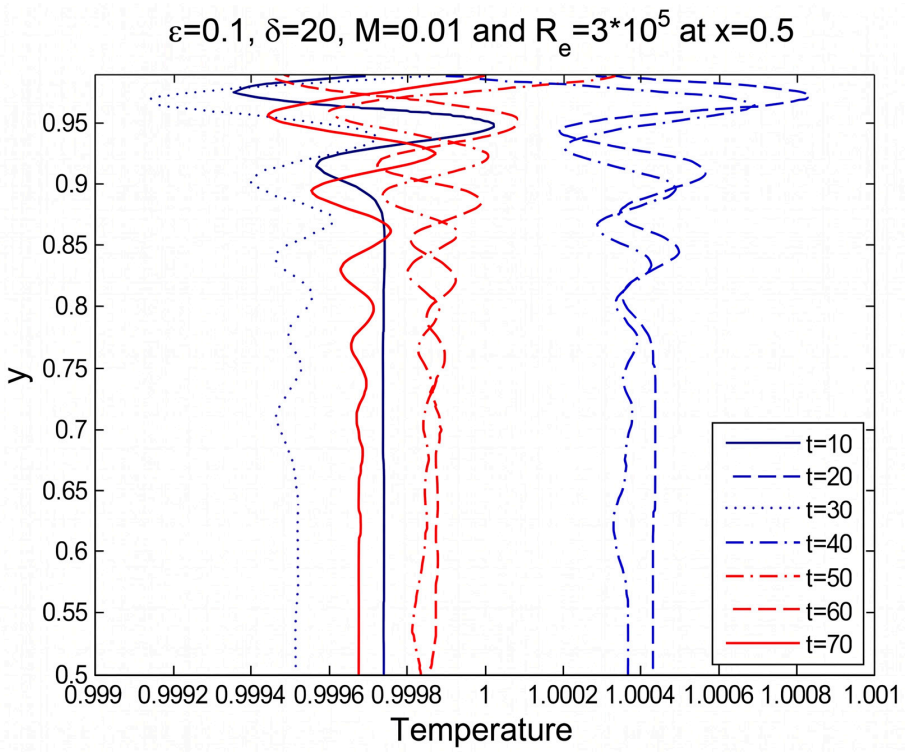


**Figure 7:** Vertical variations of temperature at the mid-length of the chamber at seven different times for the non-resonance solution.

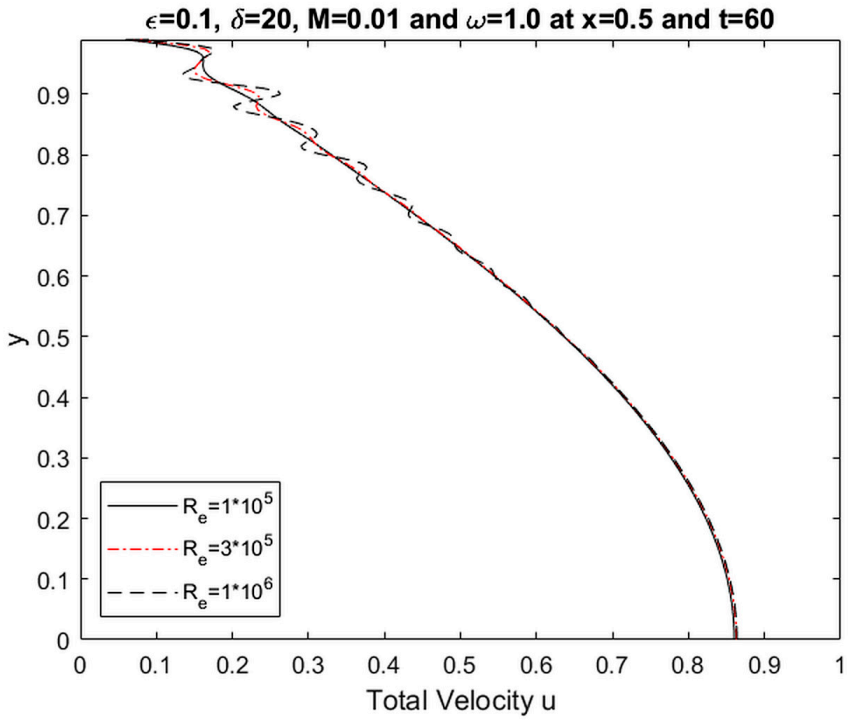


**Figure 8:** Vertical variations of the velocity at the mid-length of the chamber at three different Reynolds numbers.

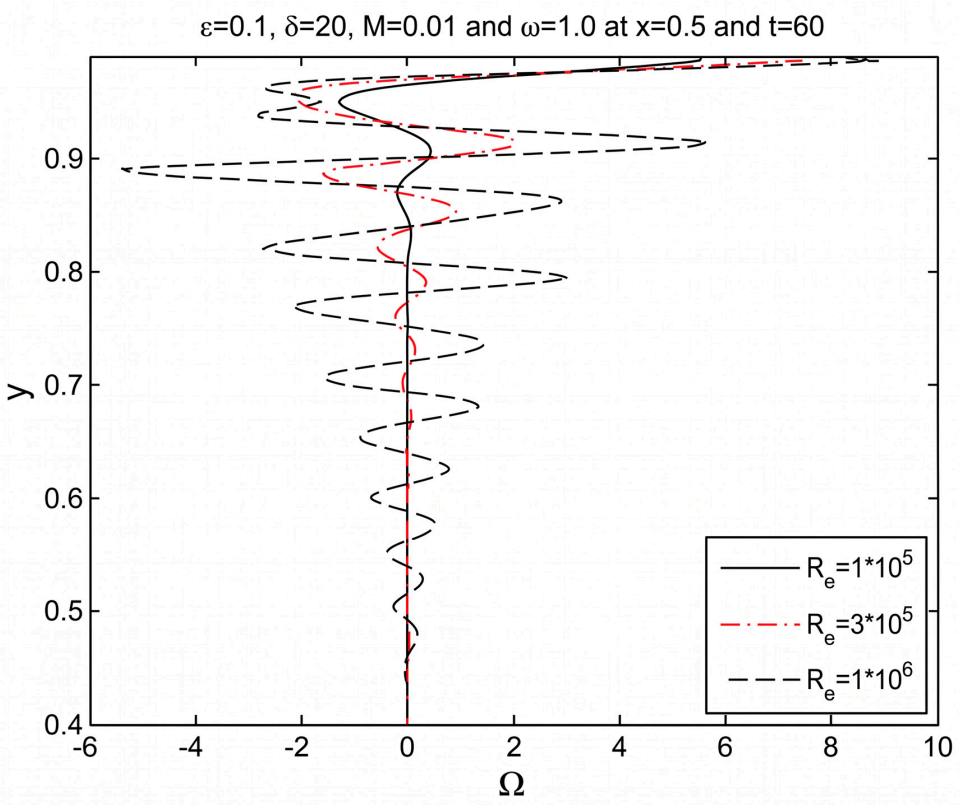


**Figure 9:** Vertical variations of the unsteady vorticity at the mid-length of the chamber at three different Reynolds numbers.

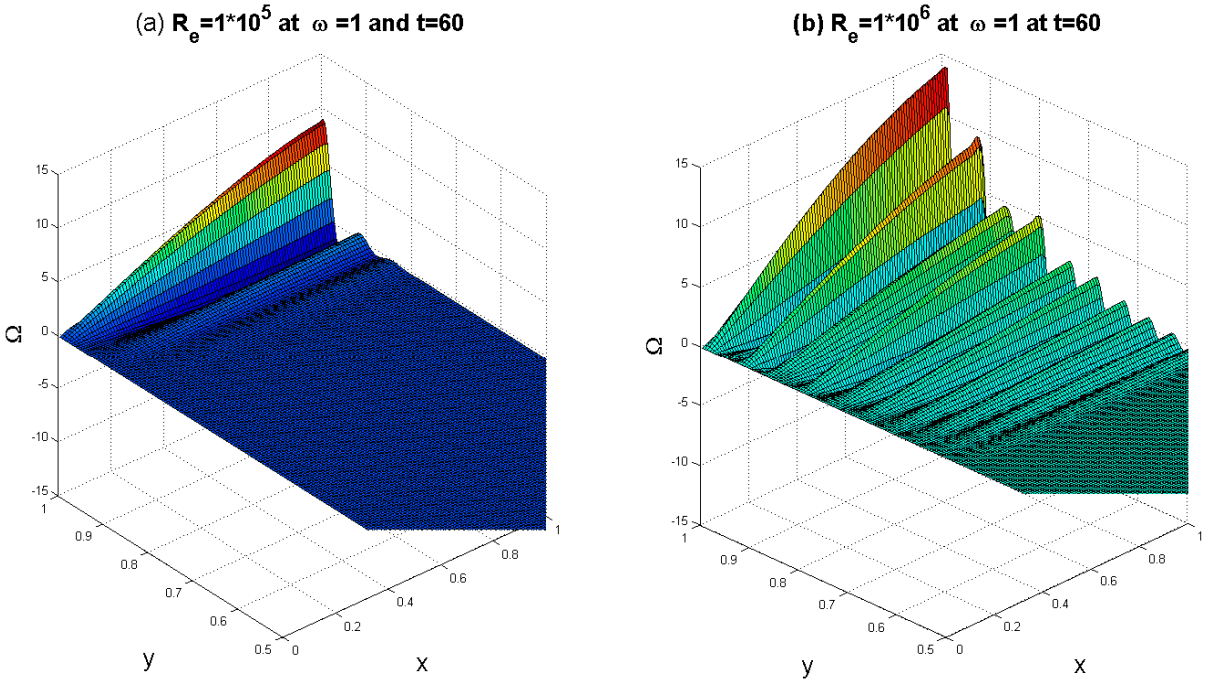


**Figure 10:** Vorticity topography for M = 0.01, δ = 20, and ε = 0.1, where t = 60 at (**a**) Re = $10^5$ (**b**) Re = $10^6$.

### *4.2 Thermal Response and Pressure Distribution*

The vertical temperature distribution corresponding to the same flow conditions is shown in Fig. 7. The temperature field responds dynamically to the rotational flow structure, exhibiting oscillatory behavior that mirrors the evolution of vorticity across the chamber cross-section. This coupling highlights the role of viscous dissipation and convective transport in redistributing thermal energy during acoustic–flow interaction.

In contrast, the pressure field exhibits negligible transverse gradients for the slender chamber configuration considered. This observation is consistent with the analytical scaling derived from the parabolized Navier–Stokes equations, which indicate that the order of magnitude of the vertical pressure gradient is $O(M^2)$ under low-Mach-number conditions. The negligible transverse pressure variation confirms that the dominant acoustic behavior remains primarily one-dimensional, even in the presence of rotational flow structures.

### *4.3 Influence of Reynolds Number*

To examine the effect of viscous transport on unsteady flow development, simulations were conducted for Re = $10^5$, $3 \times 10^5$, and $10^6$, while maintaining M = 0.01, $\alpha$ = 20, and $\varepsilon$ = 0.1 at x = 0.5. The selected Reynolds-number range represents high-Reynolds-number internal chamber flow, where viscous effects are mainly confined to thin boundary layers and inertial/acoustic effects dominate the core region. The fixed Mach number maintains consistency with the low-Mach-number asymptotic formulation, while the large aspect ratio represents a slender SRM chamber in which transverse pressure gradients remain small. The forcing amplitude was selected to generate a weakly nonlinear acoustic response without entering a strongly nonlinear or shock-dominated regime, and the mid-chamber location was used as a representative position for evaluating the interaction between incident and reflected acoustic waves.

Fig. 8 shows the vertical distribution of the velocity field for the three Reynolds numbers. As Re increases, the amplitude of oscillatory motion and flow reversal near the injection surface becomes more pronounced. This indicates that higher Reynolds numbers reduce viscous damping, allowing rotational structures generated by acoustic forcing to persist longer and penetrate further into the chamber.

Fig. 9 presents the corresponding unsteady vorticity distributions. At Re = $10^6$, significantly larger vorticity amplitudes are observed compared to Re = $10^5$. The increased Reynolds number enhances shear-layer intensity and reduces diffusive attenuation of vorticity, leading to stronger rotational motion.

The spatial structure of the rotational field is further illustrated in Fig. 10, where vorticity topography is compared for Re = $10^5$ and $10^6$ at t = 60. For the higher Reynolds number, multiple wave cycles fill the chamber cross-section, whereas only two to three cycles are visible at lower Reynolds number. The corresponding contour plots in Fig. 11 confirm that higher Reynolds numbers produce sharper gradients and more complex rotational structures.

These observations demonstrate that Reynolds number plays a critical role in governing the persistence and spatial distribution of acoustically induced vorticity. At lower Reynolds numbers, viscous diffusion suppresses rotational motion, whereas at higher Reynolds numbers, reduced damping allows sustained wave–vorticity interaction over extended time intervals.

The observed increase in vorticity amplitude and enhanced wave–flow interaction at higher Reynolds numbers is consistent with previously reported studies on acoustically induced vorticity generation and shear-layer amplification in internal flows [27–29]. These comparisons further support the physical validity of the present results and confirm that the proposed framework captures the key mechanisms governing Reynolds-number-dependent acoustic–flow coupling.

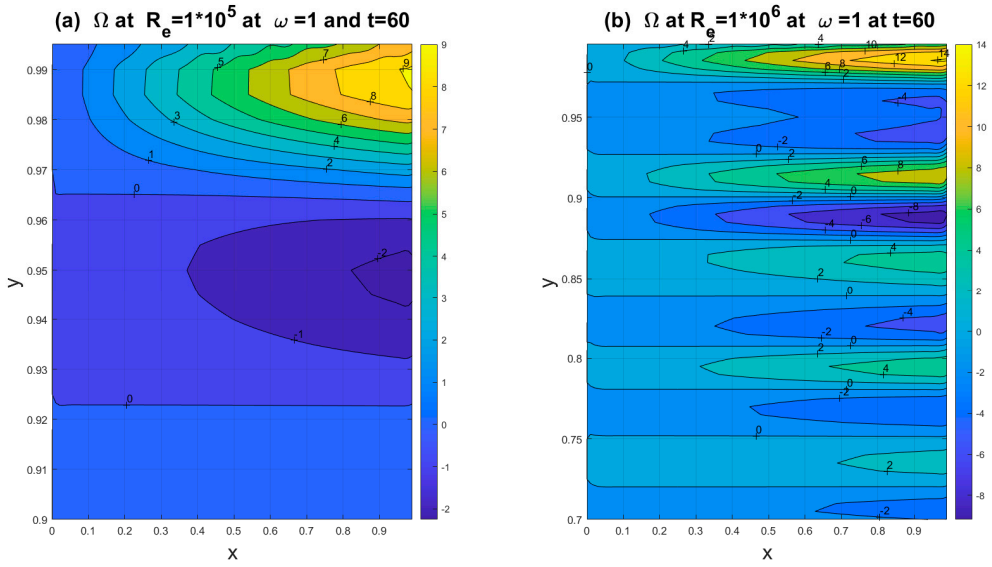


**Figure 11:** Vorticity contours for M = 0.01, δ = 20, and ε = 0.1, where t = 60 at (**a**) Re = $10^5$ (**b**) Re = $10^6$.

### *4.4 Weakly Nonlinear Effects*

The leading-order acoustic equations derived in Section 2.3 describe linear wave propagation under the assumption of small Mach number. However, higher-order asymptotic analysis indicates that nonlinear effects emerge at $O(M^3)$, contributing to intermodal interactions over longer time scales.

The computational results exhibit higher harmonic content superimposed on the primary oscillation mode, consistent with weakly nonlinear behavior predicted analytically. While quadratic nonlinear convective terms do not contribute to intermodal energy transfer at $O(M^2)$, cubic nonlinearities govern amplitude modulation and gradual distortion of the wave profile. The agreement between analytical expectations and numerical observations confirms that the adopted framework captures both linear acoustic propagation and weakly nonlinear modulation mechanisms within the chamber. The broader physical interpretation and engineering relevance of these findings are discussed in the following section.

## 5 Mechanistic Insights and Engineering Implications

The results presented in Section 4 provide more than a description of unsteady flow behavior; they reveal fundamental mechanisms governing the interaction between acoustic forcing and injected flow within slender rocket motor chambers. The combined asymptotic and computational framework enables interpretation of the internal flow response in terms of coupled wave–vorticity dynamics, where acoustic pressure oscillations act as the primary driver of rotational motion near injection surfaces. The decomposition of velocity and vorticity fields demonstrates that rotational structures do not arise independently but are generated through the interaction of oscillatory pressure gradients with the steady shear introduced by sidewall mass injection. This interaction is strongest in regions of high velocity gradient, particularly near the walls, where boundary-layer effects amplify shear-induced vorticity production.

A key mechanistic insight emerging from the present study is the decisive role of the characteristic Reynolds number in governing the persistence and spatial penetration of acoustically induced vorticity. At lower Reynolds numbers, viscous diffusion suppresses rotational structures and limits their propagation toward the chamber centerline. As the Reynolds number increases, however, diffusive damping weakens, allowing rotational motion to persist over longer times and to occupy a larger fraction of the chamber

cross-section. This behavior highlights the competition between acoustic forcing, which injects oscillatory energy into the system, and viscous dissipation, which attenuates it. The results suggest that even in nominally low-Mach-number regimes, internal flow stability characteristics can be highly sensitive to viscous scaling parameters. From a physical standpoint, this indicates that Reynolds-number-dependent amplification of rotational motion may contribute to localized shear intensification and altered acoustic energy distribution within propulsion chambers.

Another important observation is the negligible transverse pressure gradient under slender-geometry conditions. The computational results confirm the asymptotic prediction that transverse pressure variation remains of order $O(M^2)$, reinforcing the validity of the quasi-one-dimensional acoustic assumption for the pressure field. However, while the pressure field remains predominantly one-dimensional, the velocity and vorticity fields exhibit fully two-dimensional structure due to injection-induced shear and acoustic modulation. This distinction is significant because it demonstrates that simplified acoustic pressure models may remain valid even when complex rotational flow structures develop in the velocity field. Consequently, pressure-based stability assessments alone may not fully capture internal shear-layer dynamics that could influence mixing, heat transfer, or local stress distribution.

The appearance of higher harmonic content and weakly nonlinear modulation further supports the relevance of higher-order asymptotic contributions. Although quadratic nonlinear terms do not produce intermodal energy transfer at the considered order, cubic nonlinearities introduce amplitude modulation over longer time scales. The numerical results showing harmonic superposition confirm that the adopted framework captures these subtle nonlinear features without requiring fully nonlinear high-Mach-number modeling. This indicates that weakly nonlinear analysis, when combined with accurate boundary-condition implementation, can provide meaningful insight into acoustic–flow coupling mechanisms while maintaining computational efficiency.

From an engineering perspective, the findings have several implications for solid rocket motor chamber modeling and design assessment. First, the sensitivity of rotational flow intensity to Reynolds number suggests that variations in propellant mass injection rate or internal flow properties may alter the distribution of shear stresses within the chamber. Such variations could influence localized heat transfer rates and potentially affect material loading near the injection surfaces. Second, the demonstrated importance of characteristic-based boundary treatments highlights the need for accurate wave reflection modeling when simulating propulsion chambers. Spurious reflections or excessive numerical damping could obscure physically relevant wave–flow interactions and lead to inaccurate stability predictions. The ability of the present framework to maintain stable solutions over extended simulation times underscores its suitability for studying sustained oscillatory phenomena.

At the same time, it is important to acknowledge the modeling assumptions underlying the present formulation. The analysis is restricted to two-dimensional motion and assumes constant thermophysical properties. The applicability of the present asymptotic formulation is also limited to low-Mach-number acoustic motion. At higher Mach numbers, stronger coupling between pressure, density, and temperature fields, nonlinear wave steepening, and possible shock formation may occur, especially near nozzle or geometric discontinuities. Such conditions would require a fully compressible treatment without the low-Mach-number asymptotic simplifications used in the present work. Real solid rocket motor chambers involve three-dimensional effects, combustion–pressure coupling, and potentially multiphase flow behavior. The imposed exit-plane disturbance serves as a controlled surrogate for combustion-driven oscillations, but it does not represent a fully coupled combustion–acoustic instability mechanism. Therefore, the present framework should be interpreted as a mechanistic tool for analyzing instability-relevant acoustic–flow

coupling, rather than a complete predictive model for chemically driven combustion instability amplitudes. Consequently, while the present framework captures essential acoustic–flow interaction dynamics, extension to fully reactive and multiphase configurations would require additional modeling components. Recognizing these limitations strengthens the interpretive clarity of the results and delineates the scope of applicability of the present study. Although the present model does not explicitly include combustion chemistry, it captures the dominant acoustic–flow interaction mechanisms that govern instability behavior in solid rocket motor chambers. The effects of combustion are represented in an equivalent manner through steady sidewall mass injection and imposed pressure disturbances, which mimic the influence of propellant burning and unsteady forcing. This approach allows isolation of the fundamental coupling between acoustic waves and internal flow dynamics, providing physically meaningful insight while maintaining computational tractability. In addition, the present formulation is restricted to two-dimensional flow. In three-dimensional configurations, additional acoustic modes and more complex vortical structures may arise, which can influence energy transfer and spatial flow development. While the primary acoustic–flow interaction mechanisms identified in this study are expected to remain qualitatively valid, quantitative predictions such as mode amplitudes and flow structure may be affected by three-dimensional effects.

Overall, the mechanistic understanding gained from this investigation reinforces the importance of integrated analytical–computational approaches for studying propulsion-related unsteady flows. The results demonstrate that even in simplified chamber geometries, complex rotational structures and weakly nonlinear wave interactions can arise from the interplay between acoustic forcing and steady mass injection. By combining asymptotic insight with stable numerical implementation, the present framework provides a physically grounded tool for examining internal flow dynamics in rocket motor chambers and for informing future studies aimed at coupling acoustic behavior with combustion and structural response.

## 6 Conclusions

A combined asymptotic and characteristic-based computational framework has been developed and applied to investigate unsteady acoustic–flow interactions in a solid rocket motor chamber subjected to exit-plane disturbances and steady sidewall mass injection. The formulation integrates a low-Mach-number asymptotic analysis with time-accurate numerical simulation of the compressible Navier–Stokes equations, enabling consistent interpretation of acoustic wave propagation, rotational flow generation, and weakly nonlinear modulation within a unified modeling structure.

Validation against experimental measurements and previously established analytical and numerical results demonstrated that the adopted computational framework accurately reproduces pressure oscillation amplitudes and phase characteristics while maintaining numerical stability over extended simulation times. The characteristic-based boundary condition implementation was shown to reduce spurious reflections and numerical diffusion, allowing reliable simulation of multiple acoustic cycles without loss of solution fidelity.

The results revealed that exit-plane acoustic forcing, when coupled with steady sidewall mass injection, generates rotational flow structures near the injection surfaces that progressively penetrate the chamber cross-section. The decomposition of the velocity field confirmed that rotational motion arises from the interaction between oscillatory pressure gradients and steady shear layers. A systematic investigation of Reynolds number effects demonstrated that increasing Reynolds number reduces viscous damping, thereby amplifying vorticity intensity and promoting sustained wave–vorticity interaction. At lower Reynolds numbers, viscous diffusion suppresses rotational structures and limits their spatial development. These findings highlight the critical role of viscous scaling in governing internal shear dynamics under acoustically forced conditions.

The computational results further confirmed the asymptotic prediction that transverse pressure gradients remain negligible in slender chamber configurations, even when complex two-dimensional velocity and vorticity structures develop. This distinction between predominantly one-dimensional acoustic pressure behavior and two-dimensional rotational flow dynamics provides important insight into the interpretation of simplified acoustic models. In addition, the presence of higher harmonic content and amplitude modulation in the numerical results supports the relevance of weakly nonlinear contributions predicted by higher-order asymptotic analysis.

From an engineering standpoint, the study underlines the importance of accurate boundary-condition treatment and Reynolds-number scaling in predictive modeling of rocket motor chambers. While the present configuration represents a simplified two-dimensional, non-reactive system with prescribed exit-plane forcing, the framework provides a physically grounded basis for examining internal flow response to sustained acoustic excitation. The analysis clarifies the mechanisms through which injected flow and acoustic waves interact and establishes a stable computational platform for future extensions involving combustion coupling, three-dimensional effects, and more complex instability scenarios.

Overall, the present investigation demonstrates that an integrated analytical–computational approach can provide both physical insight and numerical robustness in the study of unsteady acoustic–flow interaction phenomena in propulsion-related configurations. The developed framework offers a reliable foundation for further exploration of acoustic stability behavior in solid rocket motor chambers and related engineering systems.

**Acknowledgement:** During the preparation of this work, the authors used ChatGPT 4.0 to refine writing and improve readability. The authors have reviewed and edited the AI-generated content as necessary and take full responsibility for the contents of this publication.

**Funding Statement:** This research project was funded via the Deanship of Scientific Research (DSR), King Abdulaziz University, Jeddah, Kingdom of Saudi Arabia, under grant number (D-056-829-1439). The authors wish to express their gratitude to DSR for their technical and financial support.

**Author Contributions:** Conceptualization, Abdelkarim Hegab and Faisal Albatati; methodology, Abdelkarim Hegab. and Asad A. Zaidi; software, Ahmad Hussain and Faisal Albatati; validation, Abdullah Abuhabaya and Ragab A. El-Sehiemy; formal analysis, Asad A. Zaidi and Ragab A. El-Sehiemy; investigation, Abdelkarim Hegab, Ahmad Hussain and Faisal Albatati; resources, Ragab A. El-Sehiemy; data curation, Ahmad Hussain and Ragab A. El-Sehiemy; writing—original draft preparation, Abdelkarim Hegab and Asad A. Zaidi; writing—review and editing, Ragab A. El-Sehiemy, Ahmad Hussain and Faisal Albatati; visualization, Asad A. Zaidi; supervision, Abdelkarim Hegab; project administration, Ragab A. El-Sehiemy; funding acquisition, Abdelkarim Hegab. All authors reviewed and approved the final version of the manuscript.

**Availability of Data and Materials:** Data available on request from the authors.

**Ethics Approval:** Not applicable.

**Conflicts of Interest:** The authors declare no conflicts of interest.

## Nomenclature

Abbreviations

| | |
|---|---|
| x | Dimensionless axial length $x'/L'$ |
| y | Dimensionless vertical length $y'/H'$ |
| T | Dimensionless temperature $T'/T_o'$ |
| u | Dimensionless velocity in the $x$-direction $u'/U_{zo}'$ |
| v | Dimensionless velocity in the $y$-direction $v'/(U_{zo}'/\delta)$ |

| | |
|---|---|
| p | Dimensionless pressure $p'/p_o$ |
| t | Dimensionless time $t'/t_a^{'}$, $t_a^{'} = L'/C_o^{'}$, $C_o^{©} = \left(\gamma p_o^{©}/\rho_o^{©}\right)^{1/2}$ |
| Et | Total energy $\rho[T + \gamma(\gamma-1)M^2(u^2 + (v/\delta)^2]$ |
| nx | Number of mesh points in the $x$-direction |
| ny | Number of mesh points in the $y$-direction |
| SRM | Solid rocket motor |
| LODI | Local one-dimensional inviscid |
| NSCBC | Navier-Stokes characteristic boundary condition |
| Greek Symbols | |
| Ω | Dimensionless vorticity, $\Omega = \Omega'/\left(U'_{z_o}/H'\right)$ |
| ε | Amplitude of endwall disturbances |
| λ | Chamber natural frequency |
| δ | Aspect ratio L/H |
| ρ | Dimensionless mass density $\rho'/\rho_o^{'}$ |
| Ω | Dimensionless forcing frequency |
| μ | Dynamic viscosity, Pa·s |
| χ | Viscous and conduction terms |
| ℘ | Wave amplitude |
| Subscripts | |
| os | Steady state |
| w | Wall conditions |
| n | Eigenvalues |
| 0 | First fundamentals |
| o | Reference values |
| a | Acoustic |
| v | Rotational component |
| p | Planar component |
| s | Converged steady state |
| Exponents | |
| * | Resonance conditions |
| ~ | Perturbed values |
| , | Dimensional values |
| Non-Dimensional Numbers | |
| Re & $R_{EA}$ | Reynolds number $R_e = \frac{\rho_o^{'} U_R^{'} L'}{\mu_o^{'}}$, and acoustic Reynolds number $R_{eA} = \frac{R_e}{M}$ |
| M | Characteristic Mach number $M = \frac{U_R^{'}}{C_o^{'}}$ $M \leq O(101)$ |
| Pr | Prandtl number $P_r = \frac{\mu_o^{'} C_p^{'}}{k_o^{'}}$ |

## Appendix A Asymptotic Formulation and Analytical Development

This appendix presents the detailed asymptotic expansions, intermediate governing relations, and analytical solution expressions referenced in Section 2.3. These derivations form the theoretical basis for the reduced acoustic model discussed in the main text.

### *Appendix A.1 Perturbation Expansions*

The perturbation expansions introduced for the dependent variables under the low-Mach-number assumption are given in:

$$(p, \rho, T) \sim 1 + M(P, R, \theta), (P, R, \theta) \sim \sum_{n=0}^{\infty} M^n(P_n, R_n, \theta_n), (u, v) \sim \sum_{n=0}^{\infty} M^n(u_n, v_n) \tag{A1}$$

### *Appendix A.2 Intermediate Asymptotic Relations*

Substituting the expansions of Eq. (A1) into the governing equations (Eqs. (1)–(5)) and collecting terms of equal order yields the intermediate asymptotic relations:

$$\frac{\partial R}{\partial t} + \left\{ \frac{\partial[(1+MR)u]}{\partial x} + \frac{\partial[(1+MR)v]}{\partial y} \right\} = 0 \tag{A2}$$

$$(1+MR)\left\{ \frac{\partial u}{\partial t} + M\left( u\frac{\partial u}{\partial x} + v\frac{\partial u}{\partial y} \right) \right\} = -\frac{1}{\gamma}\frac{\partial P}{\partial x} + \frac{\delta^2}{R_{eA}}\left[ \frac{\partial^2 u}{\partial y^2} + \frac{1}{\delta^2}\frac{\partial^2 u}{\partial x^2} \right] \tag{A3}$$

$$\frac{\gamma}{\delta^2}(1+MR)\left\{ \frac{\partial v}{\partial t} + M\left( u\frac{\partial v}{\partial x} + v\frac{\partial v}{\partial y} \right) \right\} = -\frac{\partial P}{\partial y} + \frac{\gamma}{R_{eA}}\left[ \frac{\partial^2 v}{\partial y^2} + \frac{1}{\delta^2}\frac{\partial^2 v}{\partial x^2} \right] \tag{A4}$$

$$(1+MR)\left\{ \frac{\partial \theta}{\partial t} + M\left( u\frac{\partial \theta}{\partial x} + v\frac{\partial \theta}{\partial y} \right) \right\} = -(\gamma-1)(1+MP)\left[ \frac{\partial u}{\partial x} + \frac{\partial v}{\partial y} \right] + \frac{\gamma\delta^2}{P_r R_{eA}}\left[ \frac{\partial^2 \theta}{\partial y^2} + \frac{1}{\delta^2}\frac{\partial^2 \theta}{\partial x^2} \right] \tag{A5}$$

$$P = \theta + R + MR\theta \tag{A6}$$

### *Appendix A.3 Leading-Order Acoustic System*

At the lowest order, the asymptotic analysis results in the linear acoustic system:

$$\frac{\partial R_o}{\partial t} + \frac{\partial u_o}{\partial x} + \frac{\partial v_o}{\partial y} = 0 \tag{A7}$$

$$\frac{\partial u_o}{\partial t} + \frac{1}{\gamma}\frac{\partial P_o}{\partial x} = 0 \tag{A8}$$

$$\frac{\partial P_o}{\partial y} = 0 \tag{A9}$$

$$\frac{\partial \theta_o}{\partial t} + (\gamma-1)\left[ \frac{\partial u_o}{\partial x} + \frac{\partial v_o}{\partial y} \right] = 0 \tag{A10}$$

$$P_o = R_o + \theta_o; P_o = \gamma R_o \tag{A11}$$

These relations are combined in the main text to obtain the pressure wave equation given in Eq. (13).

### *Appendix A.4 Leading-Order Acoustic System*

The analytical non-resonant solution for the pressure and velocity perturbations is expressed in:

$$P_o(x,t) = \frac{\varepsilon\cos(\omega x)}{\cos(\omega)}\sin(\omega t) + \sum_{n=1}^{\infty} A_n\cos(\lambda_n x)\sin(\lambda_n t) \tag{A12}$$

$$u_o(x,t) = -\frac{\varepsilon\sin(\omega x)}{\cos(\omega)}\cos(\omega t) + 2\varepsilon\omega/\gamma \sum_{n=1}^{\infty} \frac{(-1)^{n+1}}{\lambda_n^2 - \omega^2}\sin(\lambda_n x)\cos(\lambda_n t) \tag{A13}$$

These expressions describe the quasi-steady response and modal structure used for comparison with numerical simulations.

## Appendix B Characteristic-Based Boundary Condition Formulation

This appendix provides the detailed wave-mode decomposition and characteristic relations used in the numerical implementation of boundary conditions, as referenced in Sections 2.4–2.6. These expressions are omitted from the main text for clarity but are presented here in full.

### *Appendix B.1 Wave-Mode Representation*

The governing equations expressed in wave-mode form are given in:

$$\frac{\partial\rho}{\partial t} + \frac{1}{C^2}\left[\phi_2 + \frac{1}{2}(\phi_4 + \phi_1)\right] + M\frac{\partial\rho}{\partial y}v = 0 \tag{A14}$$

$$\frac{\partial u}{\partial t} + \frac{1}{2\rho C}(\phi_4 - \phi_1) + Mv\frac{\partial u}{\partial y} = \chi_x/\rho \tag{A15}$$

$$\frac{\partial v}{\partial t} + \phi_3 + Mv\frac{\partial v}{\partial y} + \frac{\delta^2}{\gamma M}\frac{1}{\rho}\frac{\partial p}{\partial y} = \chi_y/\rho \tag{A16}$$

$$\frac{\partial\hat{p}}{\partial t} + \frac{1}{2}[(\phi_4 + \phi_1)] + Mv\frac{\partial\hat{p}}{\partial y} + \gamma Mp\frac{\partial v}{\partial y} = \chi_E \tag{A17}$$

MacCormack [30] and Gottlieb & Turkel [39] has used the integrated approach as also used by Kirkkopru et al. [29] and found it suitable for describing many wave cycles and wave interaction problems. The governing equations in the wave-mode are as follows:

The definitions of the characteristic wave amplitudes are provided in:

$$\phi_1 = \lambda_1\left(\frac{1}{\gamma}\frac{\partial p}{\partial x} - M\rho C\frac{\partial u}{\partial x}\right); \lambda_1 = \frac{u}{M} - C \tag{A18}$$

$$\phi_2 = \lambda_2\left(C^2\frac{\partial\rho}{\partial x} - \frac{1}{\gamma}\frac{\partial p}{\partial x}\right); \lambda_2 = Mu \tag{A19}$$

$$\phi_3 = \lambda_3\frac{\partial v}{\partial x}; \lambda_3 = Mu \tag{A20}$$

$$\phi_4 = \lambda_4\left(\frac{1}{\gamma}\frac{\partial p}{\partial x} + M\rho C\frac{\partial u}{\partial x}\right); \lambda_4 = \frac{u}{M} + C \tag{A21}$$

where $\chi_x$ and $\chi_y$ refer to the viscous terms, and $\chi_E$ represents the mix between the viscous and conduction terms. The non-dimensional speed of sound is assigned to $C = C^{'}/C_o^{'}$. The amplitudes of the left-running waves ($\wp_1$), right-running waves ($\wp_4$), and entropy waves ($\wp_2, \wp_3$) as functions of $\lambda_i^{,}s$ are as follows:

It is important to emphasize that in in the current study both LODI and NSCBC approaches were employed to define the unknown physical boundary conditions at the head and aft ends.

### *Appendix B.2 Exit-Plane Characteristic Relations*

The characteristic relations governing the exit-plane boundary treatment are given in:

$$\phi_1 = 2\chi_E - \phi_4 - 2F(t) - 2Mv\frac{\partial\hat{p}}{\partial y} - \gamma Mp\frac{\partial v}{\partial y} \tag{A22}$$

$$\phi_2 = Mu\left(C^2\frac{\partial\rho}{\partial x} - \frac{1}{\gamma}\frac{\partial p}{\partial x}\right) \tag{A23}$$

$$\phi_3 = Mu\frac{\partial v}{\partial x} \tag{A24}$$

$$\phi_4 = \left(\frac{u}{M} + C\right)\left(\frac{1}{\gamma}\frac{\partial p}{\partial x} + M\rho C\frac{\partial u}{\partial x}\right) \tag{A25}$$

These relations determine reflected and transmitted wave amplitudes in response to the imposed pressure disturbance defined in Eq. (16).

At the exit plane, a time-dependent pressure disturbance is prescribed to excite acoustic motion within the chamber. This disturbance serves as the primary forcing mechanism and is defined through the exit-plane condition given in Eq. (16). The imposed pressure fluctuation generates right- and left-running acoustic waves that interact with the internal flow field and the chamber boundaries. Within the numerical framework, this boundary is treated using a characteristic-based formulation to ensure that wave reflection and transmission are represented accurately while minimizing non-physical numerical reflections.

The upper and lower chamber walls are modeled as impermeable boundaries with prescribed sidewall mass injection to represent steady propellant burning. No-slip velocity conditions are enforced at these

walls, and the wall temperature is maintained at a constant reference value. This treatment allows for the generation of boundary-layer vorticity and enables investigation of the interaction between injected flow and acoustically induced unsteadiness.

To implement these boundary conditions within the numerical scheme, both the Local One-Dimensional Inviscid (LODI) and Navier–Stokes Characteristic Boundary Condition (NSCBC) approaches are employed. These methods provide a systematic framework for specifying unknown boundary information based on characteristic wave propagation and have been shown to significantly reduce spurious numerical reflections during long-time simulations of unsteady compressible flows.

The treatment of the impermeable head-end boundary, which governs acoustic wave reflection within the chamber, is described separately in the following subsection.

An exit-plane pressure disturbance is specified with sinusoidal acoustic pressure at the exit-plane.

The right-running wave $\{\wp_4\}$ in Fig. 2 can be defined by Eq. (A21). The left-running wave $\{\wp_1\}$ in Fig. 3 points into the domain. The derivative of $F(t) = \varepsilon \sin(\omega t)$ is used to infer the unknown amplitude of the reflected wave $\{\wp_1\}$. Eq. (A18) suggests that the necessary condition is as follows:

The wave-mode representation of the Navier-Stokes equations is simplified by neglecting axial transport terms in $\chi_x$, $\chi_y$, and $\chi_E$. These reductions are done by other researchers in the asymptotic analysis [27,28].

The non-dimensional equations can be written in the following form:

The non-dimensional primitive variables $\rho$, $u$, and $v$ can be computationally approximated using any finite difference technique of choice. By imposing a pressure node at the exit boundary, the reflected wave in Eq. (A17) should be written as follows:

The non-dimensional variables $\rho$, $u$, and $v$ can be computationally approximated using the finite difference method, as introduced earlier.

### *Appendix B.3 Reduced Navier–Stokes Formulation*

The reduced form of the Navier–Stokes equations employed for boundary implementation is provided in:

$$\frac{\partial \rho}{\partial t} + \frac{1}{C^2}\left[Mu\left(C^2\frac{\partial \rho}{\partial x} - \frac{1}{\gamma}\frac{\partial p}{\partial x}\right) - \frac{1}{\gamma}\frac{dp}{dt}\right] + Mv\frac{\partial \rho}{\partial y} + \frac{\delta^2 M}{(\gamma-1)R_e P_r}\frac{1}{C^2}\frac{\partial^2 T}{\partial y^2} = 0 \tag{A26}$$

$$\frac{\partial u}{\partial t} + \frac{1}{\rho C}\left[\left(u + \frac{C}{M}\right)\left(\frac{1}{\gamma}\frac{\partial p}{\partial x} + M\rho C\frac{\partial u}{\partial x}\right) + \frac{1}{\gamma M}\frac{dp}{dt}\right] + Mv\frac{\partial u}{\partial y} - \frac{\delta^2}{(\gamma-1)R_e P_r}\frac{1}{\rho C}\frac{\partial^2 T}{\partial y^2} - \frac{MA^2}{R_e}\frac{1}{\rho}\frac{\partial^2 u}{\partial y^2} = 0 \tag{A27}$$

$$\frac{\partial v}{\partial t} + M\left(u\frac{\partial v}{\partial x} + v\frac{\partial v}{\partial y}\right) = 0 \tag{A28}$$

$$p = 1 + \varepsilon\sin(\omega t) \tag{A29}$$

$$\phi_1 = 2\chi_E - \phi_4 \tag{A30}$$

$$\phi_2 = Mu\left(C^2\frac{\partial\rho}{\partial x} - \frac{1}{\gamma}\frac{\partial p}{\partial x}\right), \phi_3 = Mu\frac{\partial v}{\partial x} \text{ and } \phi_4 = \left(\frac{u}{M} + C\right)\left(\frac{1}{\gamma}\frac{\partial p}{\partial x} + M\rho C\frac{\partial u}{\partial x}\right) \tag{A31}$$

$$\frac{\partial\rho}{\partial t} + Mu\frac{\partial\rho}{\partial x} - \frac{Mu}{\gamma C^2}\frac{\partial p}{\partial x} + Mv\frac{\partial\rho}{\partial y} + \frac{\delta^2 M}{(\gamma-1)R_e P_r}\frac{1}{C^2}\frac{\partial^2 T}{\partial y^2} = 0 \tag{A32}$$

$$\frac{\partial u}{\partial t} + \frac{1}{\rho C}\left[\left(u + \frac{C}{M}\right)\left(\frac{1}{\gamma}\frac{\partial p}{\partial x} + M\rho C\frac{\partial u}{\partial x}\right)\right] + Mv\frac{\partial u}{\partial y} - \frac{\delta^2}{(\gamma-1)R_e P_r}\frac{1}{\rho C}\frac{\partial^2 T}{\partial y^2} - \frac{M\delta^2}{R_e}\frac{1}{\rho}\frac{\partial^2 u}{\partial y^2} = 0 \tag{A33}$$

$$\frac{\partial v}{\partial t} + M\left(u\frac{\partial v}{\partial x} + v\frac{\partial v}{\partial y}\right) = 0 \tag{A34}$$

$$\frac{dp}{dt} = 0 \tag{A35}$$

### *Appendix B.4 Head-End Characteristic Relations*

The impermeable head-end boundary condition and its associated characteristic relations are given in:

$$\phi_4 = \phi_1 \tag{A36}$$

and the remaining conditions are the following:

$$\phi_1 = -c\left(\frac{1}{\gamma}\frac{\partial p}{\partial x} + M\rho C\frac{\partial u}{\partial x}\right) \tag{A37}$$

$$\phi_2 = 0 \text{ and } \phi_3 = 0 \tag{A38}$$

Eqs. (A31)–(A34) can be written in a non-dimensional form as follows:

$$\frac{\partial\rho}{\partial t} - M\rho\frac{\partial u}{\partial x} + \frac{1}{\gamma C}\frac{\partial p}{\partial x} + M\frac{\partial\rho v}{\partial y} = 0 \tag{A39}$$

$$\frac{\partial u}{\partial t} = 0 \tag{A40}$$

$$\frac{\partial v}{\partial t} + Mv\frac{\partial v}{\partial y} = 0 \tag{A41}$$

$$\frac{\partial p}{\partial t} - c\frac{\partial p}{\partial x} + M\rho C\frac{\partial u}{\partial x} + \gamma Mp\frac{\partial v}{\partial y} - \frac{\gamma\delta^2 M}{(\gamma-1)P_r R_e}\frac{\partial^2 T}{\partial y^2} \tag{A42}$$

These expressions complete the NSCBC/LODI boundary implementation adopted in the numerical simulations.

## References


1. Li X, Chen Z, Li X, Xu B, Wang S. Experimental study on submerged nozzle damping characteristics of solid rocket motor. Aerospace. 2024;11(9):759. [CrossRef].
2. Panchal D, Sharma R, Rana S, Vohra Y, Khan S, Tuteja D, et al. *In vitro* microbubble nucleation and sanal flow choking induced combustion instabilities in liquid rocket propulsion. In: Proceedings of the AIAA Aviation Forum and Ascend; 2025 Jul 21–25; Las Vegas, NV, USA. [CrossRef].
3. Volkov K. Simulation of particulate flows in combustion chambers of solid rocket motors with multiscale model. Acta Astronaut. 2026;238:1342–53. [CrossRef].
4. Liu Y, Liu P, Wang Z, Ao W, Xu G, Guan Y. Numerical investigation of combustion instability in a liquid rocket engine: Interaction effect between hydrodynamics and acoustic mode. Aerosp Sci Technol. 2023;143:108711. [CrossRef].
5. Muro LE, Godínez FA, Valdés R, Montoya R. How might neural networks improve micro-combustion systems? Energies. 2026;19(2):326. [CrossRef].
6. Abdolahipour S, Moomivand M, Shams Taleghani A. Effect of crossflow jet injection on induced aerodynamic loads between tandem surfaces in supersonic flow using SBES. Aerosp Sci Technol. 2026;174:111921. [CrossRef].
7. Sharma A, De A, Kumar SS. Numerical investigation of supercritical combustion dynamics in a multi-element LOx–methane combustor using flamelet-generated manifold approach. Phys Fluids. 2023;35(11):115125. [CrossRef].
8. Liang X, Yang L, Wang G, Li J. Hopf bifurcation analysis of the combustion instability in a liquid rocket engine. Aerospace. 2022;9(10):593. [CrossRef].
9. Francois L. Multiphysical modelling and simulation of the ignition transient of complete solid rocket motors [dissertation]. Paris, France: Institut Polytechnique de Paris; 2022.
10. Wajeeh-ul-Hassan S, Arif M, Basit MA, Basit R, Aslam MN. Numerical solution of steady nonlinear differential equations for compressible flow through a spinning convergent divergent nozzle. Int J Mod Phys B. 2025;39(4):2540004. [CrossRef].
11. Modise K, Magalakwe G. An internal flow and heat transfer inside a solid rocket motor combustion chamber; A Lie symmetry approach. Therm Sci Eng Prog. 2022;32:101237. [CrossRef].
12. Eckstein A. Numerical investigation of liquid fuel injection and combustion modeling for hypersonic air-breathing propulsion using RANS and LES approaches [master's thesis]. West Lafayette, IN, USA: Purdue University; 2025.
13. Price EW. Experimental solid rocket combustion instability. Symp Int Combust. 1965;10(1):1067–82. [CrossRef].
14. Margolis SB. Nonlinear stability of combustion-driven acoustic oscillations in resonance tubes. J Fluid Mech. 1993;253:67–103. [CrossRef].
15. Erickson R, Markopoulos N, Zinn B. Finite amplitude acoustic waves in variable area ducts. In: Proceedings of the 39th Aerospace Sciences Meeting and Exhibit; 2001 Jan 8–11; Reno, NV, USA. [CrossRef].
16. Merkli P, Thomann H. Thermoacoustic effects in a resonance tube. J Fluid Mech. 1975;70(1):161–77. [CrossRef].
17. Rudenko OV, Hedberg CM, Enflo BO. Nonlinear standing waves in a layer excited by the periodic motion of its boundary. Acoust Phys. 2001;47(4):452–60. [CrossRef].
18. Wang M, Kassoy DR. Nonlinear oscillations in a resonant gas column: An initial-boundary-value study. SIAM J Appl Math. 1995;55(4):923–51. [CrossRef].
19. García-Schäfer JE, Liñán A. Longitudinal acoustic instabilities in slender solid propellant rockets: Linear analysis. J Fluid Mech. 2001;437:229–54. [CrossRef].

20. Disselhorst JHM, Van Wijngaarden L. Flow in the exit of open pipes during acoustic resonance. J Fluid Mech. 1980;99(2):293–319. [CrossRef].
21. Sileem AA, Nasr M. An experimental study on finite amplitude oscillations in ducts: The effect of adding variable area part to the open end of constant-area resonant tube. Alex Eng J. 2003;42(4):397–409.
22. Mortell MP, Seymour BR. The evolution of resonance: A multiscale approach to the effect of nonlinearity, frequency dispersion and geometry. Math Model Nat Phenom. 2019;14(4):403. [CrossRef].
23. Albatati FA, Hegab AM, Rady MA, Abuhabaya AA, El-Behery SM. Turbulent flow characteristics in a model of a solid rocket motor chamber with sidewall mass injection and end-wall disturbance. Math Probl Eng. 2021;2021(1):9978102. [CrossRef].
24. Vétel J, Plourde F, Kim SD. Amplification of shear layer instability by vorticity generation at an injecting wall. AIAA J. 2004;42(1):35–46. [CrossRef].
25. Han L, Li J, Zhao D, Gu X, Ma B, Wang N. Effects of baffle designs on damping acoustic oscillations in a solid rocket motor. Aerosp Sci Technol. 2021;115:106827. [CrossRef].
26. Ji S, Wang B, Zhao D. Numerical analysis on combustion instabilities in end-burning-grain solid rocket motors utilizing pressure-coupled response functions. Aerosp Sci Technol. 2020;98:105701. [CrossRef].
27. Zhao Q, Staab PL, Kassoy DR, Kirkkopru K. Acoustically generated vorticity in an internal flow. J Fluid Mech. 2000;413:247–85. [CrossRef].
28. Staab PL, Zhao Q, Kassoy DR, Kirkkopru K. Coexisting acoustic-rotational flow in a cylinder with axisymmetric sidewall mass addition. Phys Fluids. 1999;11(10):2935–51. [CrossRef].
29. Kirkkopru K, Kassoy DR, Zhao Q. Unsteady vorticity generation and evolution in a model of a solid rocket motor. J Propuls Power. 1996;12(4):646–54. [CrossRef].
30. MacCormack RW. A numerical method for solving the equations of compressible viscous flow. AIAA J. 1982;20(9):1275–81. [CrossRef].
31. Roga S. Modern rocket propulsion: A critical review of technological advances and ongoing challenges. Int J Chem Reactor Eng. 2025;23(10):1179–96. [CrossRef].
32. Meiirbekov M, Nurguzhin M, Ismailov M, Janikeyev M, Kadyrov Z, Omarbayev M, et al. A comprehensive review of application techniques for thermal-protective elastomeric ablative coatings in solid rocket motor combustion chambers. Technologies. 2026;14(2):77. [CrossRef].
33. Venegas O, Hernández C, Fernández C. Review on the fundamentals and recent developments in rotating detonation engines experimental and numerical setups. Propuls Power Res. 2025;14(4):595–610. [CrossRef].
34. Xu G, Wang B, Jin B, Wang Z, Liu P. Numerical study of triggered thermoacoustic instability driven by linear and nonlinear combustion response in a solid rocket motor. Phys Fluids. 2024;36(3):034110. [CrossRef].
35. Huo C, Xu H, Hu J, Luo T. Numerical study on pressure oscillations in a solid rocket motor with backward step configuration under two-phase flow interactions. Aerospace. 2024;11(12):1054. [CrossRef].
36. Li Z, Abdellatif A, Yang R, Jofre L, Capuano F. Navier–Stokes characteristic boundary conditions for real fluids with kinetic-energy- and pressure-equilibrium-preserving schemes. J Comput Phys. 2025;535:114035. [CrossRef].
37. Xi Y, Gao J, Wu Z, Zhang B, Yang L, Xia J. Pressure oscillation and suppression method of large-aspect-ratio solid rocket motors. Chin J Aeronaut. 2025;38(4):103275. [CrossRef].
38. Pierce AD. Acoustics: An introduction to its physical principles and applications. Berlin/Heidelberg, Germany: Springer; 2019. [CrossRef].
39. Gottlieb D, Turkel E. Dissipative two-four methods for time-dependent problems. Math Comput. 1976;30(136):703–23. [CrossRef].
40. Hegab A, Albatati F, Algarni M. Laminar and turbulent characteristics of the acoustic/fluid dynamics interactions in a slender simulated solid rocket motor chamber. Comput Model Eng Sci. 2021;127(2):437–68. [CrossRef].
41. Hegab AM. Vorticity generation and acoustic resonance of simulated solid rocket motor chamber with high wave number wall injection. Comput Fluids. 2009;38(6):1258–69. [CrossRef].
42. Hegab AM, Sait HH, Hussain A. Impact of the surface morphology on the combustion of simulated solid rocket motor. Math Probl Eng. 2015;2015(1):485302. [CrossRef].